



HAL
open science

A multi-technique characterisation of cronstedtite synthetized by iron-clay interaction in a step by step cooling procedure

Isabella Pignatelli, Enrico Mugnaioli, J. Hybler, Régine Mosser-Ruck, Michel Cathelineau, Nicolas Michau

► **To cite this version:**

Isabella Pignatelli, Enrico Mugnaioli, J. Hybler, Régine Mosser-Ruck, Michel Cathelineau, et al.. A multi-technique characterisation of cronstedtite synthetized by iron-clay interaction in a step by step cooling procedure. *Clays and Clay Minerals*, 2013, 61 (4), pp.277-289. 10.1346/CCMN.2013.0610408 . hal-01876737

HAL Id: hal-01876737

<https://hal.univ-lorraine.fr/hal-01876737v1>

Submitted on 18 Sep 2018

HAL is a multi-disciplinary open access archive for the deposit and dissemination of scientific research documents, whether they are published or not. The documents may come from teaching and research institutions in France or abroad, or from public or private research centers.

L'archive ouverte pluridisciplinaire **HAL**, est destinée au dépôt et à la diffusion de documents scientifiques de niveau recherche, publiés ou non, émanant des établissements d'enseignement et de recherche français ou étrangers, des laboratoires publics ou privés.

Clays and Clay Minerals

A multi-technique characterisation of cronstedtite synthesized by iron-clay interaction in a step by step cooling procedure

--Manuscript Draft--

Manuscript Number:	CCM-748R1
Full Title:	A multi-technique characterisation of cronstedtite synthesized by iron-clay interaction in a step by step cooling procedure
Short Title:	Synthesis of cronstedtite by iron-clay interaction
Article Type:	Article
Section/Category:	
Keywords:	Cronstedtite; MDO polytypes; radioactive waste storage; experimental iron-clay interaction.
Corresponding Author:	Isabella Pignatelli GeoRessources Vandœuvre-lès-Nancy, FRANCE
Corresponding Author Secondary Information:	
Corresponding Author's Institution:	GeoRessources
Corresponding Author's Secondary Institution:	
First Author:	Isabella Pignatelli
First Author Secondary Information:	
Order of Authors:	Isabella Pignatelli Enrico Mugnaioli, doctoral degree Jiri Hybler, doctoral degree Régine Mosser-Ruck, doctoral degree Michel Cathelineau, professor Nicolas Michau, doctoral degree
Order of Authors Secondary Information:	
Abstract:	<p>The cooling of steel containers in radioactive waste storages has been simulated by an original step by step experiment from 90°C to 40°C. Among newly formed clay minerals observed in run products, cronstedtite has been undoubtedly identified by different analytical techniques (XRD, TEM and SEM). This is the first time that cronstedtite is so abundant and well-crystallized in an iron-clay interaction experiment. The supersaturation of experimental solutions with respect to cronstedtite is due to the availability of Fe and Si in solution, as a result of the dissolution of iron metal powder, quartz and in a minor amount other silicates. Cronstedtite crystals are characterized by various morphologies: pyramidal (truncated or not) with a triangular base and conic with a rounded or hexagonal cross-section. The pyramidal crystals occur more frequently and their polytypes (2M1, 1M, 3T) have been identified by selected area electron diffraction (SAED) patterns and by automated diffraction tomography (ADT). Cronstedtite is stable within the 90°-60°C temperature range. At temperature $\leq 50^\circ\text{C}$, cronstedtite crystals show evidences of alteration.</p>

24 crystallized in an iron-clay interaction experiment. The supersaturation of experimental
25 solutions with respect to cronstedtite is due to the availability of Fe and Si in solution, as a
26 result of the dissolution of iron metal powder, quartz and in a minor amount other silicates.
27 Cronstedtite crystals are characterized by various morphologies: pyramidal (truncated or not)
28 with a triangular base and conic with a rounded or hexagonal cross-section. The pyramidal
29 crystals occur more frequently and their polytypes ($2M_1$, $1M$, $3T$) were identified by selected
30 area electron diffraction (SAED) patterns and by automated diffraction tomography (ADT).
31 Cronstedtite is stable within the 90°-60°C temperature range. At temperature $\leq 50^\circ\text{C}$,
32 cronstedite crystals show evidences of alteration.

33 **KEYWORDS**

34 Cronstedtite, MDO polytypes, radioactive waste storage, experimental iron-clay interaction.

36 **INTRODUCTION**

37 This paper presents a multi-technique characterization of cronstedtite crystals formed from an
38 original experimental procedure on iron-clay interactions. The choice of this experiment was
39 driven by the need to evaluate the effects of a progressive decrease in temperature expected
40 during the cooling of nuclear waste containers. First of all, a mineralogical assemblage was
41 obtained after heating at 90°C an iron-clay mixture. Its retrograde evolution was thus
42 simulated by a step by step cooling experiment between 90°C and 40°C. For the first time,
43 single crystals of well-crystallized cronstedtite were observed in run products and accurately
44 characterized. The temperature stability domain of cronstedtite was estimated on the basis of
45 experimental evidence (occurrence and instability of crystals) and compared to literature data.
46 This detailed mineralogical characterization of newly formed cronstedtite is useful to improve
47 databases of the thermodynamic models.

BACKGROUND

49 Cronstedtite is a T-O or 1:1 phyllosilicate, with a general formula $(\text{Fe}^{2+}_{3-x} \text{Fe}^{3+}_x)(\text{Si}_{2-x}\text{Fe}^{3+}_x)\text{O}_5(\text{OH})_4$, with $0 < x < 0.8$ (Geiger *et al.*, 1983; Smrčok *et al.*, 1994; Hybler *et al.*, 2000; Hybler *et al.*, 2002; Kogure *et al.*, 2002), close to the initial ideal formula $(\text{Fe}^{2+}_2 \text{Fe}^{3+})(\text{SiFe}^{3+})\text{O}_5(\text{OH})_4$ proposed by Hendricks (1939). Chemical analyses of cronstedtite also show that the octahedrally coordinated iron can be replaced by other cations as Mg^{2+} , Mn^{2+} , Al^{3+} (Frondel, 1962; Geiger *et al.*, 1983) and that the tetrahedral sites can also contain Al^{3+} (Geiger *et al.*, 1983; Hybler *et al.*, 2002). Cronstedtite forms a solid solution with greenalite $(\text{Fe}^{2+}, \text{Fe}^{3+}, \text{Mg}, \square)_3(\text{Si}, \text{Al})_2\text{O}_5(\text{OH})_4$ (Guggenheim *et al.*, 1982), another Fe-rich layer silicate, from which it differs by the presence of ferric iron in tetrahedral coordination.

58 Like other trioctahedral T-O phyllosilicates, standard polytypes of cronstedtite can be classified in four subfamilies, identical with Bailey's (1969) groups: A ($1M$, $2M_1$, $3T$ polytypes), B ($2O$, $2M_2$, $6H$), C ($1T$, $2T$, $3R$) and D ($2H_1$, $2H_2$, $6R$), on the basis of the interlayer shift and of the rotation between succeeding layers (Bailey, 1969). In the Order-Disorder theory (Dornberger-Schiff and Āurovič, 1975) these polytypes are defined as *MDO* polytypes (Maximum Degree Order). Among them, only 8 polytypes have been reported for cronstedtite in the literature (Table 1): $1T$, $1M$, $2H_1$, $2H_2$, $2M_1$, $2T$, $3T$ and $6R$ (Steadman and Nuttall, 1963, 1964). One non-standard or non-MDO polytype has also been found by Frondel (1962) in a cronstedtite sample coming from the Cornucopia mine (Nye Country, Nevada) and it was indicated by the Ramsdell symbol $9R$.

68 In terrestrial environments, cronstedtite was found in sulfide veins as a low-temperature hydrothermal mineral, associated with siderite, pyrite, sphalerite and quartz (Frondel, 1962) and also in metamorphosed massive sulphide deposits (Lopez-Garcia *et al.*, 1992). In Australian banded iron-formations of lower metamorphic grade, Gole (1980 a, b) reported the coexistence of greenalite with another mineral that he identified as probable cronstedtite.

73 Cronstedtite occurs also in carbonaceous chondrites both in fine-grained rims and matrices as
74 product of aqueous alteration on the parent body (Müller *et al.*, 1979; Barber, 1981; Burbine
75 and Burns, 1994, Browning *et al.*, 1996; Lauretta *et al.*, 2000; Zega and Buseck, 2003;
76 Miyahara *et al.*, 2008)

77 A few experimental works reported the formation of T-O Fe-rich minerals of the serpentine
78 group. Odinite (R^{3+} , R^{2+} , \square)₃(Si_{2-x} Al_x)O₅(OH)₄ and hexagonal crystals of cronstedtite as run
79 products of dioctahedral smectites-iron metal interactions at 80° C were reported by Lantenois
80 (2003), Lantenois *et al.* (2005) and Lanson *et al.* (2012). Under similar experimental
81 conditions, Fe-rich T-O phyllosilicates were described as “berthierine type” phases with
82 general formula (R^{2+} , R^{3+} , \square)₃(Si_{2-x}, Al_x)O₅(OH)₄ (Brindley, 1982) or “Fe-rich 7 Å clays” or
83 “serpentine-like minerals” (Wilson *et al.*, 2006; Perronnet *et al.*, 2007; Mosser-Ruck *et al.*,
84 2010; Jodin-Caumon *et al.*, 2010; de Combarieu *et al.*, 2011; Jodin-Caumon *et al.*, 2012;
85 Rivard *et al.*, 2013), sometimes close to the greenalite end-member (Pierron, 2011). The
86 numerous designations of low temperature Fe-rich phyllosilicates found in literature were
87 explained by the difficulty of their identification. They often appeared as highly disordered or
88 nanocrystalline phases (Schlegel *et al.*, 2008) or as small crystal associated with Si-Al-Fe
89 gels (Perronnet *et al.*, 2008), and they can coexist with other Fe-rich phases in experimental
90 run products.

91

92 **MATERIALS AND METHODS**

93 *Starting material*

94 The starting clay rich rock used in our experiments is a claystone from the Callovo-Oxfordian
95 formation (noted COx) of the Paris Basin, a formation investigated for future waste storage in
96 the underground research laboratory (URL) at the Meuse/Haute-Marne site of Bure (France).

97 The claystone contains on average 41% of clay minerals (illite, mixed-layered illite/smectite,

98 being the predominant clay minerals, and minor amounts of kaolinite and chlorite), 25% of
99 quartz, 31% of carbonates (calcite and minor dolomite) and the remaining 3% consist of
100 pyrite, phosphates, K-feldspar and organic matter (Rousset, 2002; Gaucher *et al.*, 2004).
101 The starting products (experimental solutions and clays) were prepared under inert argon
102 atmosphere, using a solution of 0.0207 mol/kg NaCl and 0.0038 mol/kg CaCl₂ (pH = 6.4) and
103 1 g of claystone grinded in a mortar to obtain a liquid/solid mass ratio of 10. Metal iron was
104 added to the system as a powder (500 mg; average grain size ~ 40 μm) and as two plates with
105 dimensions of nearly 3x6x1mm³ (iron powder/CO_x mass ratio of 0.5). The starting mixture
106 was put in Parr® non-stirred pressure vessels made of Teflon® with capacity of ~20 ml.
107 Seven vessels were heated in a furnace at 90(±2)° C for 6 months and then the temperature
108 was decreased every month by steps of 10°C until 40°C. At each temperature, a vessel was
109 removed from the oven. After quenching and opening of each vessel, the solid run products
110 were dried under an argon flux at room temperature.

111

112 *ManoCalcimeter*

113 Quantitative analysis of carbonates was performed in the Museum National d'Histoire
114 Naturelle (MNHN) using a Mélières manoCalcimeter (MCM) on 200 mg of bulk rock sample
115 powder (see Ledéseret *et al.*, 2009). MCM uses a “Karbonat-Bombe” which is a simple
116 apparatus composed of glass flask and a high precision manometer (Dunn, 1980). This
117 method gives a direct measurement of carbonates for rocks containing only calcite or
118 aragonite (CaCO₃). The MCM is built to give a 100 mg value when 1 millimole of CO₂ is
119 emitted during chemical attack of 100 mg (# 1 millimole) of CaCO₃ by 8N hydrochloric acid.
120 Nevertheless, molecular weight of carbonates varying with their chemical composition and
121 100 mg of pure dolomite for example provokes the emission of 1.085 millimole of CO₂. As a
122 consequence, the values read on the MCM must be corrected as a function of the amount of

123 the different carbonates identified by XRD. Calibration was performed using pure calcite
124 crystals; uncertainty precision is around 0.5 wt.%.

125

126 *X-ray diffraction*

127 The data were collected at room temperature with a D8 Bruker diffractometer, using the
128 CoK α radiation ($\lambda = 1.7902 \text{ \AA}$), 35kV accelerating voltage and 45mA intensity. The Bruker
129 DIFFRAC^{plus} package was used for the data acquisition and analysis.

130 XRD patterns of randomly oriented powder were obtained, using a scan step of 0.035° (2θ),
131 exposure time of 3 seconds, $2\theta_{\min} = 3^\circ$ and $2\theta_{\max} = 54^\circ$.

132

133 *Scanning electron microscopy (SEM)*

134 The secondary electron (SE) and backscattered electrons (BSE) images of the cronstedtite
135 crystals were obtained with an accelerating voltage of 15 kV using a cold FEG Hitachi S-
136 4800. The lateral resolution of FEG-SEM is about 1 nm for SE images. The crystals of
137 cronstedtite analysed were collected on the iron plates, deposited on the carbon adhesive
138 sticks and then carbon coated. Energy dispersive X-ray spectra (EDXS) were performed to
139 identify the chemical elements present in crystals.

140

141 *Transmission electron microscopy (TEM) and Energy-dispersive X-ray (EDX) spectroscopy*

142 TEM images and EDX analyses were carried out at 200 kV using a Philips CM20 microscope
143 with a point resolution of 0.27 nm equipped with Si-Li detector. The TEM specimens were
144 prepared dispersing the $< 2 \mu\text{m}$ fraction powders in ethanol under ultrasonic and evaporating a
145 drop of the suspension on a carbon network-like holey support film placed on a 200 mesh
146 copper grid (Euromedex-Mundolcheim, France). The chemical composition of run products
147 was determined using energy dispersive X-Ray spectroscopy (EDXS). EDX spectra were

148 recorded by means of a PGT spectrometer mounted on CM20 Philips microscope operated at
149 200 kV and equipped with an ultrathin window X-Ray detector. The analyses were carried out
150 in nanoprobe mode with a probe diameter of 10 nm using K_{AB} determined from clay standards
151 with similar thickness.

152 Selected area electron diffraction (SAED) patterns were recorded at 120 kV using a Philips
153 CM120 microscope with a Digistar Nanomegas CCD camera.

154

155 *Automated electron diffraction tomography (ADT)*

156 3D electron diffraction data were also collected by a Tecnai F30 S-Twin microscope
157 operating at 300 kV. Powdered sample (< 2 μm fraction) was dispersed in ethanol, sonified
158 and sprayed on a carbon-coated copper grid by a UIS250v Hielscher sonifier, according to the
159 procedure described by Mugnaioli *et al.* (2009). Data collection was carried out by a
160 combination of automated diffraction tomography (ADT) and precession electron diffraction
161 (PED) (Kolb *et al.*, 2007, 2008; Mugnaioli *et al.*, 2009). Nano electron diffraction patterns
162 were collected in steps of 1° in a tilt range up to $-60/+60^\circ$. Data processing, 3D reciprocal
163 space reconstruction and cell parameter determination were performed by ADT3D software.

164

165 *Analysis of solutions*

166 The pH of each run solution was measured with a combination of silver/sulfide electrode in
167 glove box after cooling at room temperature and 0.025 μm filtration. The electrode was
168 calibrated using reference buffer solutions certified by PTB and NIST Institutes with pH 4, 7
169 and 10. The run solutions were diluted ten times in 2% vol. HNO_3 and analyzed by
170 inductively coupled plasma optical emission spectroscopy (ICP-OES) at LIMOS laboratory to
171 determine the concentration of dissolved Si and Fe.

172

RESULTS

173

174 *ManoCalcimeter and X-ray diffraction*

175 XRD patterns of untreated mixed iron-CO_x sample and run samples are shown in Figure 1.
176 Calcite reflection at 3.03 Å is unchanged on the 90°C to 40°C patterns, indicating that this
177 mineral is unaffected by the cooling. As the manoCalcimeter results confirm that calcite
178 content is constant (10±1 wt%) in all samples, XRD patterns were normalized to calcite
179 reflection (3.03 Å). Intensities of quartz, iron metal and T-O-T phyllosilicates (mica and illite)
180 reflections decrease on XRD pattern of 90°C experiment. This decrease is emphasized on the
181 other XRD patterns corresponding to 80°C-40°C experiments. At the same time, intensities of
182 magnetite and 7 Å phyllosilicates increase. This indicates a strong dissolution of quartz and
183 iron metal (more than 70% for both phases) and partial destruction of T-O-T phyllosilicate
184 layers. The XRD results highlight the increase of the 7 Å clays amount in run products but
185 don not allow to accurately distinguish T-O minerals because of their similar d_{hkl} values.

186

187 *Scanning electron microscopy*

188 The SEM analyses show that dominant 7 Å clays obtained in the 90°C experiment are iron-
189 rich and have different morphologies (Figure 2). Pyramidal (truncated or not) crystal with a
190 triangular base and conic crystals were observed. The last ones have rounded or hexagonal
191 cross-sections (Figure 2a-b). The different morphologies still coexist down to 70° C (Figure
192 2c-d), then at lower temperatures pyramidal shape becomes the dominant morphology (Figure
193 2e-f).

194

195 *Transmission electron microscopy*

196 *Energy dispersive X-ray analyses and TEM imaging*

197 EDX analyses were performed on isolated particles of < 2 μm fraction powders. From the
198 EDX results, structural formulae have been calculated on the basis of 7 oxygens and the
199 Fe³⁺/Fe²⁺ ratio has been adjusted to set the occupation of the octahedral sites to 3. The
200 compositions (expressed as a.p.f.u., *i.e.* atom per formula unit) of 28 pyramidal crystals and 5
201 conic crystals formed at 90° and 80° C are reported in Tables 2 and 3. The mean formula is:



203 The difference in the chemistry of crystals with respect to their morphology is not significant
204 considering the standard deviation (Tables 2 and 3). The Si-deficit and the presence of ferric
205 iron in the tetrahedral sites allow to identify these two types of crystals as cronstedtite.

206 TEM images show that the higher crystallinity of the newly formed iron rich clays was
207 observed in 70°C and 60°C run products (Figure 3) and also that this mineral becomes
208 unstable at temperature ≤ 50°C as demonstrated by alteration of its faces (Figure 4). At 40°C
209 very rare relict crystals of altered cronstedtite were still observed.

210

211 *SAED patterns and ADT/PED investigations: determination of cronstedtite polytypes*

212 Because of their great abundance in run product, well-shaped pyramidal cronstedtites formed
213 during 70°C experiment were chosen to identify their MDO polytypes following the
214 procedure described by Āurovič (1981). According to the Order-Disorder (OD) theory
215 (Dornberger-Schiff, 1956, 1964, 1966, and 1979), the superposition vectors and rotations (of
216 almost identical 1:1 layers) needed to obtain the four possible subfamily structures, are as
217 follows: ±**a**_i/3 for subfamily A; ±**b**/3 or zero for subfamily C; ±**a**_i/3, and ±**b**/3 or zero
218 combined with 180° rotation for subfamilies B and D, respectively (Dornberger-Schiff, 1964;
219 Bailey, 1969). The **a**_i and **b** are hexagonal and orthohexagonal unit cell vectors, respectively.

220 It follows that the subfamily sublattice corresponding to the Fourier transform of subfamily
221 structure is formed by reflections with $k = 3n$ (in orthohexagonal indexing, or $h-k = 3n$ in

222 hexagonal indexing). These reflections are common to all polytypes belonging to the same
223 subfamily and are consequently called *subfamily reflections*. Whereas the reflection having k
224 $\neq 3n$ (in orthohexagonal indexing, or $h-k \neq 3n$ in hexagonal indexing) are typical of each
225 polytypes and are said *non-family* or *polytype reflections*. Usually diffraction patterns of two
226 orthogonal reciprocal lattice sections are enough to identify a MDO polytype: the diffraction
227 pattern of $(h0l)^*$ (hhl in hexagonal indexing) containing the subfamily reflections allowing to
228 determine the subfamily and the diffraction pattern from $(0kl)^*$ ($\bar{h}hl$ in hexagonal indexing),
229 containing both subfamily and polytype reflection useful to identify the polytype (Ďurovič,
230 1997). In non-trigonal and non-hexagonal polytypes, however, the diffraction pattern of the
231 $(0kl)^*$ plane is different from that of $(h0l)^*$, because they are not symmetry equivalent
232 (Ďurovič, priv. comm.). In order to determine such polytypes to a certainty the $(0kl)^*$ planes
233 should be recorded and checked as well.

234 The spots distribution on experimental electron diffraction 2D patterns were compared with
235 the identification diagrams for MDO polytypes of cronstedtite described in literature
236 (Ďurovič, 1997, Hybler *et al.*, 2008), and with diffraction patterns theoretically calculated
237 with aid of the DIFK91 program (Smrčok and Weiss, 1993).

238 SAED patterns of several pyramidal cronstedtites underline that they are all $1M$ polytypes.
239 The spot distribution along the $11l$ reciprocal lattice row on $(hhl_{\text{hex}})^*$ plane indicates that these
240 crystals belong to the subfamily (Bailey's group) A (Figure 5). Moreover the spot distribution
241 on $(h0l_{\text{hex}})^*$ and $(0kl_{\text{hex}})^*$ planes corresponds to MDO group II and I respectively (Figure 6).
242 Both are in agreement with theoretically calculated patterns. $1M$ cronstedtite polytype is very
243 rare and generally occurs intergrown to the $3T$ polytype and strongly disordered (Ďurovič,
244 1997).

245 Three ADT data sets were collected on different crystals and reconstructed in 3D diffraction
246 volumes. The first acquisition, coming from a nicely shaped pyramidal crystal (Figure 7a),

247 shows diffuse scattering along c^* for both $h0l_{\text{hex}}$ and hhl_{hex} reflections, so that no polytypic
248 identification can be made (Figure 7b).

249 The second acquisition comes from a crystal with pyramidal shape, where two corners are
250 truncated and one not (Figure 8a). Remarkably the not-truncated corner is characterized by
251 diffuse disorder, while the rest of the crystal delivers a mostly coherent diffraction consistent
252 with the subfamily A and to MDO group III, *i.e.* $2M_1$ polytype (Figure 8b-d). The cell is C -
253 centred monoclinic with parameters $a = 5.5 \text{ \AA}$, $b = 9.6 \text{ \AA}$, $c = 14.4 \text{ \AA}$, $\beta = 97.4^\circ$. Systematic
254 absences for reflections $h0l$ with $l \neq 2n$ suggest the presence of a glide plane c perpendicular
255 to the b axis. This is in agreement with the space group Cc found by Steadman and Nuttall
256 (1964) for this polytype. Worth noting is that $2M_1$ polytype of cronstedtite is also very rare in
257 nature (Đurovič, 1997). The presence of diffuse scattering along c^* testifies anyway to a
258 certain degree of disorder even in most ordered parts of the crystal.

259 The third acquisition highlights the presence of another polytype belonging to the subfamily
260 A and MDO group IV, *i.e.* $3T$ polytype (Figure 9a-b). The cell is hexagonal with parameters a
261 $= 5.5 \text{ \AA}$, and $c = 21.4 \text{ \AA}$. Intensity distribution suggests a trigonal symmetry (Laue class $\bar{P}3$
262 or $\bar{P}31m$), consistent with the space group $P3_1$ reported in literature (Steadman and Nuttall,
263 1963; Smrčok *et al.*, 1994).

264

265 *Solution chemistry*

266 The characterization of run solutions shows that the mean pH value is 7.47 ± 0.16 and that Si
267 concentration varies between 7 and 11 ppm in function of the experiments (Figure 10). Quartz
268 solubility at each run temperature has been calculated by PHREEQC geochemical software
269 package V2.17 (Parkhurst and Appelo, 1999) and the associated LLNL database (Johnson *et*
270 *al.*, 2000). Si concentration is under the quartz solubility curve in run solution of experiment
271 carried out in the temperature range of 90° - 60° C, whereas at 50° C the Si concentration is on

272 the quartz solubility curve. Finally, the Si concentration slightly increases in the last run
273 solution (40° C). Fe concentration in the experimental solutions is very low (< 1 ppm) or
274 under limit detection.

275

276 **DISCUSSION AND CONCLUSIONS**

277 The significant decrease of quartz, T-O-T phyllosilicates and iron metal intensity reflections
278 on X-ray diffraction patterns indicates that these phases were dissolved releasing Si and Fe in
279 experimental solutions. Quartz dissolution is confirmed by Si concentration measured in run
280 solutions which is lower than that at equilibrium with quartz between 90°-60°C (Figure 10).
281 At this temperature range, cronstedtite is formed together with other 7 Å clays. As iron
282 content in run solutions is lower than 1 ppm or under limit of detection (< 5 ppb), it is all
283 incorporated in newly formed minerals (cronstedtite, magnetite and other iron-rich silicates).
284 At temperatures of 50° and 40°C measured Si content is respectively equal and higher than
285 that at equilibrium with quartz, preventing the precipitation of cronstedtite. Thanks to the
286 original step by step cooling procedure presented in this paper, the stability range of
287 cronstedtite with respect to the temperature was determined. Between 90°C to 60°C
288 cronstedtite appears to be stable and 50°C corresponds to the lower limit of cronstedtite
289 stability as confirmed by crystal alteration (Results §). The upper limit is $\geq 90^\circ\text{C}$ but it cannot
290 be accurately determined. Surely, no cronstedtite has ever been observed in similar
291 experiments carried out on the same claystone (COx) at higher temperatures of 150°C and
292 300°C (Pierron, 2011).

293 The cooling experiments from 90°C to 60°C favored the development of crystals with
294 pyramidal (truncated or not) morphologies and enhanced crystallinity. Pyramidal crystals
295 analyzed by TEM show different polytypic sequences and various degrees of disorder. The
296 identified polytypes, all belonging to the subfamily A, are $2M_1$ and $1M$ together with $3T$.

297 According to Hybler *et al.* (2008), these two monoclinic polytypes are very rare whereas 3*T*
298 polytype is relatively abundant in nature. The mean formula for pyramidal polytypes is in
299 good agreement with that reported by Kogure *et al.* (2002) for cronstedtite of subfamily A,
300 even if our crystals contain small amounts of Al and Mg (Table 2). Conic crystals of
301 cronstedtite occur with pyramidal ones only in 90°C and 80°C experiments. The coexistence
302 of these two different morphologies may be due to changes of the supersaturation degree
303 during growth. When the supersaturation decreased, the crystals take a polyhedral habitus
304 bounded by flat faces (Sunagawa, 2005), changing the morphology from conic to pyramidal.
305 According to the literature, one can also suppose that conic crystals may be cronstedtite
306 polytypes belonging to the C or D subfamilies (Fron del, 1962; Kogure *et al.*, 2001; Hybler *et*
307 *al.*, 2002). The co-occurrence of one of these two subfamilies with the subfamily A has been
308 already observed (C + A or D + A subfamilies) by Hybler *et al.* (2008). The detailed study of
309 conic crystals is the object of an investigation under development and will be discussed in a
310 future work.

311

312 *Comparison with cronstedtite from chondrites*

313 Several studies about the formation conditions of cronstedtite were carried out on
314 carbonaceous chondrites in which this mineral is the dominant component (Dyl *et al.*, 2010).
315 Cronstedtite crystals in meteorites are often small, platy and characterized by high degree of
316 stacking disorder (Müller *et al.*, 1979; Laurretta *et al.*, 2000; Zega and Buseck., 2003). For this
317 reason it is difficult to identify their polytypes. Nevertheless, Müller *et al.* (1979) and Zaga
318 and Buseck (2003) found mostly 1*T* polytype and Müller *et al.* (1979) reported that the
319 second more frequent polytype is 1*M*. Even if the conditions of cronstedtite formation in
320 meteorites are close to those of our experiments (presence of metal Fe, neutral-alkaline
321 solution, reducing conditions), 1*T* polytype was not observed in our run products. Mass-

322 transfer and reaction-path calculations simulating aqueous alteration in chondrites propose
323 that the upper limit of cronstedtite stability is 90°-100°C according to Schulte and Shock
324 (2004) and McAlister and Kettler (2008). These calculations were done with the hypothesis
325 that the activity of silica in solution is close to quartz saturation. This disagrees with our
326 chemical data obtained on experimental solution which indicate that the activity of aqueous
327 silica is under quartz saturation between 90°C and 70°C.

328

329 *Comparison with run products in similar experimental conditions*

330 The results presented in this paper have shown that the occurrence of cronstedtite is restricted
331 to the 90°C-50°C domain of temperature. But at 90°C, in the 6 months experiment,
332 cronstedtite is not so abundant and its crystallinity degree is low. Is it a kinetic or temperature
333 effect? To answer this question, our results were compared to those of similar experiments
334 carried out on the same starting materials. Rivard (2011) and Pierron (2011) used the same
335 claystone (COx of the Meuse/Haute-Marne site of Bure) at 90°C for 9 months but using
336 slightly different liquid/solid mass ratio (20 and 10 respectively) and iron powder/COx mass
337 ratio (0.2 and 0.1 or 1 respectively). They observed the crystallization of iron-rich T-O clays
338 with a composition between odinite, berthierine and greenalite (Figure 11). No cronstedtite
339 have been reported by these authors. These results seem to confirm that the formation of
340 cronstedtite is strongly favored by a lower temperature range, and maybe by a temperature
341 decrease.

342

343 *Concluding remarks*

344 In clay formations which may be host deep-geological radioactive waste disposal, a first
345 increase of temperature to 90° C close to the containers and then followed by a cooling is
346 expected. Our experiments simulated the mineralogical evolution of the iron-clay system

347 around the steel containers during a cooling between 90° and 40° C. They showed that the
348 composition of iron rich T-O clays stable at 90°C (close to odinite, greenalite or berthierine)
349 will evolve toward cronstedtite during the cooling. This result has to be taken into account in
350 the understanding of complex interaction in glass-iron-clay systems.

351

352 **ACKNOWLEDGMENTS**

353 The authors thank L. Mouton and J. Ghanbaja respectively for SEM and TEM images and
354 analyses at SCMEM laboratory (Université de Lorraine, France). U. Kolb is warmly thanked
355 for providing access to TEM laboratory at the Institut für Physikalische Chemie, Johannes
356 Gutenberg Universität. The authors also wish to thank M. Klementova and L. Palatinus for
357 acquisition and processing of SAED patterns, L. Truche for helpful discussion. This research
358 was financially supported by ANDRA – Agence Nationale pour la gestion des Déchets
359 Radioactifs (French national agency for the management of radioactive wastes).

360

361 **REFERENCES**

- 362 Bailey, S.W. (1969) Polytypism of trioctahedral 1:1 layer silicates. *Clays and Clay Minerals*,
363 **17**, 355-371.
- 364 Bailey, S.W. (1988) Odinite, a new dioctahedral-trioctahedral Fe³⁺-rich 1:1 clay mineral. *Clay*
365 *Minerals*, **23**, 237-247.
- 366 Barber, D.J. (1981) Matrix phyllosilicates and associated minerals in C2M carbonaceous
367 chondrites. *Geochimica et Cosmochimica Acta*, **45**, 945-970.
- 368 Brindley, G.W. (1982) Chemical compositions of berthierines – A review. *Clays and Clay*
369 *Minerals*, **30**, 153-155.

370 Browning, L.B., McSween, H.Y. Jr. and Zolensky, M.E. (1996) Correlated alteration effects
371 in CM carbonaceous chondrites. *Geochimica et Cosmochimica Acta*, **60**, 2621-2633.

372 Burbine, T.H. and Burns, R.G. (1994) Questions concerning the oxidation of the ferrous iron
373 in carbonaceous chondrites. *Lunar Planetary Science*, **XXV**, 199-200.

374 de Combarieu, G., Schlegel, M.L., Neff, D., Foy, E. Vantelon, D., Barboux, P. and Gin, S.
375 (2011) Glass-iron-clay interactions in a radioactive waste geological disposal : an
376 integrated laboratory-scale experiment. *Applied Geochemistry*, **26**, 65-79.

377 Dornberger-Schiff, K. (1956) On Order-Disorder Structures (OD-Structures). *Acta*
378 *Crystallographica*, **9**, 593-601.

379 Dornberger-Schiff, K. (1964) Grundzüge einer Theorie von OD-Strukturen aus Schichten.
380 Abh. dtsh. Akad Wiss Berlin, Kl. f. Chem., 3, 107 p.

381 Dornberger-Schiff, K. (1966) Lehrgang über OD-Strukturen. Berlin: Akademie-Verlag, 135
382 p.

383 Dornberger-Schiff, K. (1979) OD structures- a game and a bit more. *Kristall Und Technik*, **14**,
384 1027-1045.

385 Dornberger-Schiff, K. and Ďurovič, S. (1975) OD-interpretation of kaolinite-type structure-I:
386 symmetry of kaolinite packets and their stacking possibilities. *Clays and Clay Minerals*,
387 **23**, 219-229.

388 Dunn, D.A. (1980). Revised techniques for quantitative calcium carbonate analysis using the
389 "Karbonat-Bombe," and comparisons to other quantitative carbonate analysis methods.
390 *Journal of Sedimentary Research*, **50**, 631-636.

391 Ďurovič, S. (1981) OD-Charakter, Polytypie und Identifikation von Schichtsilikaten.
392 *Fortschritte der Mineralogie*, **59**, 191-226.

393 Ďurovič, S. (1997) Cronstedtite-1M and co-existence of 1M and 3T polytypes. *Ceramics –*
394 *Silikáty*, **41** (3), 98-104.

395 Dyl, K.A., Manning, C.E. and Young, E.D. (2010) The implication of the cronstedite in
396 water-rich planetesimals and asteroids. Astrobiology Science Conference 2010, League
397 City, Texas.

398 Frondel, C. (1962) Polytypism in cronstedtite. *American Mineralogist*, **47**, 781-783.

399 Gaucher, E., Robelin, C., Matray, J.M., Négrel, G., Gros, Y., Heitz, J.F., Vinsot, A., Rebours,
400 H., Cassagnabère, A. and Bouchet, A. (2004) ANDRA underground research laboratory :
401 interpretation of the mineralogical and geochemical data acquired in the Callovian-
402 Oxfordian formation by investigative drilling. *Physics and Chemistry of the Earth*, **29**,
403 55-77.

404 Geiger, C.A., Henry, D.L., Bailey, S.W. and Maj, J.J. (1983) Crystal structure of cronstedtite-
405 $2H_2$. *Clays and Clay Minerals*, **31**, 97-108.

406 Gole, M.J. (1980a) Low-temperature retrograde minerals in metamorphosed Archean banded
407 iron-formations, Western Australia. *Canadian Mineralogist*, **18**, 205-214.

408 Gole, M.J. (1980b) Mineralogy and petrology of very-low metamorphic grade Archean
409 banded iron-formations, Weld Range, Western Australia. *American Mineralogist*, **65**, 8-
410 25.

411 Guggenheim, S., Bailey, S.W., Eggleton, R.A. and Wilkes, P. (1982) Structural aspects of
412 greenalite and related minerals. *Canadian Mineralogist*, **20**, 1-18.

413 Hendricks, S.B. (1939) Random Structures of layer minerals as illustrated by cronstedtite
414 ($2FeO \cdot Fe_2O_3 \cdot SiO_2 \cdot 2H_2O$). Possible iron content of kaolin. *American Mineralogist*, **24**,
415 529-539.

416 Hybler, J., Ďurovič, S. and Kogure, T. (2008) Polytypism in cronstedtite. *Acta*
417 *Crystallographica*, **A64**, C498-499.

418 Hybler, J., Petříček, V., Ďurovič, S. and Smrčok, L. (2000) Refinement of the crystal structure
419 of cronstedtite-1T. *Clays and Clay Minerals*, **48**, 331-338.

420 Hybler, J., Petříček, V., Fábry, J. and Ďurovič, S. (2002) Refinement of the crystal structure
421 of cronstedtite- $2H_2$. *Clays and Clay Minerals*, **50**, 601-613.

422 Jodin-Caumon, M.C., Mosser-Ruck, R., Randi, A., Pierron, O., Cathelineau, M. and Michau,
423 N. (2012) Mineralogical evolutions of a claystone after reaction with iron under thermal
424 gradient. *Clays and Clay Minerals*, **60**, 5, 443-455.

425 Jodin-Caumon, M.C., Mosser-Ruck, R., Rousset, D., Randi, A., Cathelineau, M. and Michau,
426 N. (2010) Effect of a thermal gradient on iron-clay interactions. *Clays and Clay Minerals*,
427 **58**, 5, 667–681.

428 Johnson, L., Anderson, G., Parkhurst, D. (2000) Database from ‘thermo.com.V8.R6.230’
429 Prepared at Lawrence Livermore National Laboratory (Revision: 1.11).

430 Kogure, T., Hybler, J. and Ďurovič, S. (2001) A HRTEM study of cronstedtite : determination
431 of polytypes and layer polarity in trioctahedral 1 :1 phyllosilicates. *Clays and Clay*
432 *Minerals*, **49**, 310-317.

433 Kogure, T., Hybler, J. and Yoshida, H. (2002) Coexistence of two polytypic groups in
434 cronstedtite from Lostwithiel England. *Clays and Clay Minerals*, **50**, 504-513.

435 Kolb, U., Gorelik, T. and Otten, M.T. (2008) Towards automated diffraction tomography.
436 Part II – Cell parameter determination. *Ultramicroscopy*, 108, 763-772.

437 Kolb, U., Gorelik, T., Kübel, C. and Otten, M.T. (2007) Towards automated diffraction
438 tomography : Part I – Data acquisition. *Ultramicroscopy*, **107**, 507-513.

439 Lanson, B., Lantenois, S. Van Aken, P.A., Bauer, A. and Plançon, A. (2012) Experimental
440 investigation of smectite interaction with metal iron at 80°C : structural characterization
441 of newly formed Fe-rich phyllosilicates. *American Mineralogist*, **97**, 864-871.

442 Lantenois, S. (2003) Réactivité fer metal/smectites en milieu hydraté à 80°C, Ph.D. thesis,
443 Université d’Orleans, Orleans, 220 pp.

444 Lantenois, S., Lanson, B., Muller, F., Bauer, A., Jullien, M. and Plançon, A. (2005)
445 Experimental study of smectite interaction with metal Fe at low temperature: 1. Smectite
446 destabilization. *Clays and Clay Minerals*, **53**, 597-612.

447 Lauretta, D.S., Hua, X. and Buseck, P.R. (2000) Mineralogy of fine-grained rims in the ALH
448 81002 CM chondrite. *Geochimica et Cosmochimica Acta*, **64**, 3263-3273.

449 Ledéser B., Hébert R., Grall C., Genter A., Dezayes C., Bartier D. and Gérard A. (2009).
450 Calcimetry as a useful tool for a better knowledge of flow pathways in the Soultz-sous-
451 Forêts Enhanced Geothermal System, *Journal of Volcanology and Geothermal Research*,
452 **181**, 106-114.

453 López García, J.A., Manteca, J.I., Prieto, A.C. and Calvo, B. (1992) Primera aparición en
454 España de cronstedtita. Caracterización estructural. *Boletín de la Sociedad Española de*
455 *Mineralogía*, **15-1**, 21-25.

456 McAlister, J.A. and Kettler, R.M. (2008) Metastable equilibria among dicarboxylic acids and
457 the oxidation state during aqueous alteration on the CM2 chondrite parent body.
458 *Geochimica et Cosmochimica Acta*, **72**, 233-241.

459 Miyahara, M., Uehara, S., Ohtani, E., Nagase T., Nishijima, M., Vashaei, Z. and Kitagawa, R.
460 (2008) The anatomy of altered chondrules and FGRs covering hem in a CM chondrite by
461 FIB-TEM-STEM. *Lunar Planetary Science*, **XXXIX**, 199-200.

462 Mosser-Ruck, R., Cathelineau, M., Guillaume, D. and Charpentier, D. (2010) Effects of
463 temperature, pH, and iron/clay and liquid/clay ratios on experimental
464 conversion of dioctahedral smectite to berthierine, chlorite, vermiculite, or saponite.
465 *Clays and Clay Minerals*, **58**, 280-291.

466 Mugnaioli, E., Gorelik, T. and Kolb, U. (2009) “Ab initio” structure solution from electron
467 diffraction data obtained by a combination of automated diffraction tomography and
468 precession technique. *Ultramicroscopy*, **109**, 758-765.

469 Müller, W.F., Kurat, G. and Kracher, A. (1979) Chemical and crystallographic study of
470 cronstedtite in the matrix of the Cochabamba (CM2) carbonaceous chondrite. *Tschermaks*
471 *Mineralogische und Petrographische Mitteilungen*, **26**, 293-304.

472 Parkhurst, D.L., Appelo, C.A.J. (1999) User's guide to PHREEQC (Version 2). A Computer
473 Program for Speciation, Batch-reaction, One-dimensional Transport, and Inverse
474 Geochemical Calculations. U.S. Geological Survey Water-Resources Investigations
475 Report 99-4259, 312 pp.

476 Perronnet, M., Jullien, M., Villiéras, F., Raynal, J., Bonnin, D. and Bruno, G. (2008) Evidence
477 of a critical content in Fe(0) on FoCa7 bentonite reactivity at 80°C. *Applied Clay Science*,
478 **38**, 187-202.

479 Perronnet, M., Villiéras, F., Jullien, M., Razafitianamaharavo, A., Raynal, J. and Bonnin, D.
480 (2007) Towards a link between the energetic heterogeneities of the edge of smectites and
481 their stability in the context of metallic corrosion. *Geochimica et Cosmochimica Acta*, **71**,
482 1463-1479.

483 Pierron, O. (2011) Interactions eau-fer-argilite : rôle des paramètres Liquide/Roche,
484 Fer/Argilite, Température sur la nature des phases minérales, Ph.D. thesis, Université
485 Henri Poincaré, Nancy, 226 pp.

486 Rivard, C. (2011) Contribution à l'étude de la stabilité des minéraux constitutifs de l'argilite
487 du Callovo-Oxfordien en présence de fer à 90°C, Ph.D. thesis, Institut National
488 Polytechnique de Lorraine, Nancy, 338 pp.

489 Rivard, C., Pelletier, M., Michau, N., Razafitianamaharavo, A., Bihannic, I., Abdelmoula, M.,
490 Ghanbaja, J. and Villiéras, F. (2013) Berthierine-like mineral formation and stability
491 during the interaction of kaolinite with metallic iron at 90 °C under anoxic and oxic
492 conditions. *American Mineralogist*, **98**, 163-180.

493 Rousset, D. (2002) Etude de la fraction argileuse de séquence sédimentaires de la Meuse et du
494 Gard. Reconstruction de l'histoire diagénétique et des caractéristiques physico-chimiques
495 des cibles, Ph.D. thesis, Université Louis Pasteur, Strasbourg, 269 pp.

496 Schlegel, M.L., Bataillon, C., Benhamida, K., Blanc, C., Menut, D. and Lacour, J. (2008)
497 Metal corrosion and argillite transformation at the water-saturated, high-temperature iron-
498 clay interface : a microscopic-scale study. *Applied Geochemistry*, **23**, 2619-2633.

499 Schulte, M. and Schock, E. (2004) Coupled organic synthesis and mineral alteration on the
500 meteorite parent bodies. *Meteoritic and Planetary Science*, **39**, 1577-1590.

501 Smrčok, L., Ďurovič, S., Petříček, V. and Weiss, Z. (1994) Refinement of the crystal structure
502 of cronstedtite-3T. *Clays and Clay Minerals*, **42**, 544-551.

503 Smrčok, L., Weiss, Z (1993) DIFK91: a program for the modelling of powder diffraction
504 patterns on a PC. *Journal of Applied Crystallography* 26, 140-141.

505 Steadman, R. and Nuttall, P.M. (1963) Polymorphism in cronstedtite. *Acta Crystallographica*,
506 **16**, 1-8.

507 Steadman, R. and Nuttall, P.M. (1964) Further polymorphism in cronstedtite. *Acta*
508 *Crystallographica*, **17**, 404-406.

509 Sunagawa, I. (2005) *Crystals. Growth, morphology and perfection*, Cambridge University
510 Press.

511 Wilson, J., Cressey G., Cressey, B., Cuadros, J., Vala Ragnarsdottir, K., Savage, D. and
512 Shibata, M. (2006) The effect of iron on montmorillonite stability. (II) Experimental
513 investigation. *Geochimica et Cosmochimica Acta*, **70**, 323-336.

514 Zega, T.J. and Buseck, P.R. (2003) Fine-grained-rim mineralogy of the Cold Bokkeveld CM
515 chondrite. *Geochimica et Cosmochimica Acta*, **67**, 1711-1721.

516
517

518

TABLES

519 **Table 1.** Polytypes of trioctahedral T-O phyllosilicates and cronstedtite (literature data).

520

521 **Table 2.** Cation contents (a.p.f.u, *i.e.* atom per formula unit) in 28 pyramidal crystals of
522 cronstedtite formed between 90° and 80°C.

523

524 **Table 3.** Cation contents (a.p.f.u) in 5 conic crystals of cronstedtite formed between 90° and
525 80°C.

526

527

FIGURES CAPTIONS

528 **Figure 1.** XRD patterns of run samples collected from 90°C to 40°C experiments and
529 untreated mixed iron-CO_x sample (Chl = chlorite, T-O-T Ph = T-O-T phyllosilicates, Qz =
530 quartz).

531

532 **Figure 2.** a) SEM image of cronstedtite crystals with different morphologies in 90°C
533 experiment and a relative EDX spectrum (b). c), d) BSE images of conic (in circle) and
534 pyramidal cronstedtites in 70°C experiment. e), f) BSE and SE images of pyramidal crystals
535 of cronstedtite in 60°C experiments.

536

537 **Figure 3.** TEM micrographs of conic (a, b) and pyramidal cronstedtites (c, d) formed between
538 90° and 80°C.

539

540 **Figure 4.** TEM image of unstable cronstedtite crystal in 50°C experiment.

541

542 **Figure 5.** SAED pattern of $(hhl_{\text{hex}})^*$ plane for $1M$ polytype. Note, that the pattern contains
543 also few weak parasitic spots of an unidentified phase.

544

545 **Figure 6.** SAED patterns of $(h0l_{\text{hex}})^*$ and $(0kl_{\text{hex}})^*$ planes for $1M$ polytype.

546

547 **Figure 7.** First ADT acquisition. a) TEM image of the pyramidal crystal selected for ADT
548 acquisition. b) ADT 3D diffraction reconstruction (along an oblique view) showing the
549 diffuse scattering along c^* .

550

551 **Figure 8.** Second ADT acquisition. a) TEM image of the truncated crystal. The area pointed
552 by the black arrow was affected by diffuse disorder, while the area pointed by the white arrow
553 was selected for ADT acquisition. b) ADT 3D diffraction reconstruction viewed along a^* .
554 White arrows point the reflections $h0l$ with $l \neq 2n$ extinct due the c -glide plane. c) ADT 3D
555 diffraction reconstruction viewed along b^* . d) ADT 3D diffraction reconstruction viewed
556 along c^* . An extraneous reflection coming from another crystal is marked with a circle. Note
557 that these are projections of a 3D diffraction volume and not conventional 2D electron
558 diffraction patterns.

559

560 **Figure 9.** Third ADT acquisition. a) TEM image of the crystal selected for the acquisition
561 (indicated by a black arrow). b) ADT 3D diffraction reconstruction viewed along a^* showing
562 the 21.4 Å periodicity.

563

564 **Figure 10.** Si concentration (ppm) in run solutions vs experimental temperature.

565

566 **Figure 11.** Chemical composition of the most evolved newly formed T-O clays plotted in a
567 Si-Al-Fe_{tot} ternary diagram. Experiments of this study are represented by diamonds.
568 Pierron's experiments (2011) and Rivard's experiments (2011) are represented respectively
569 by squares and triangles. Gr: greenalite (Fe³⁺_{0.45}Fe²⁺_{1.9}Mg_{0.3}□_{0.35})Si_{2.0}O₅(OH)₄ (Guggenheim
570 *et al.*, 1982); Od: odinite (Al_{0.15}Fe³⁺_{1.2}Fe²⁺_{0.35}Mg_{0.7}□_{0.6})(Si_{1.85}Al_{0.15})O₅(OH)₄ (Bailey, 1988);
571 Be: berthierine (Al_{0.96}Fe³⁺_{0.22}Fe²⁺_{1.49}Mg_{0.17}□_{0.17})(Si_{1.15}Al_{0.85})O₅(OH)₄ (Brindley, 1982); Cr:
572 cronstedtite (Fe³⁺_{0.84}Fe²⁺_{2.16})(Si_{1.16}Fe³⁺_{0.84})O₅(OH)₄ (Kogure *et al.*, 2002).

573

574

Table 1

Polytypes of trioctahedral T-O phyllosilicates	<i>MDO polytypes of trioctahedral T-O phyllosilicates</i>				Authors
	A	B	C	D	Bailey (1969)
	<i>1M, 2M₁, 3T</i>	<i>2O, 2M₂, 6H</i>	<i>1T, 2T, 3R</i>	<i>2H₁, 2H₂, 6R</i>	
	<i>MDO polytypes of cronstedtites</i>				
	<i>1M, 2M₁, 3T</i>		<i>1T, 2T</i>	<i>2H₁, 2H₂, 6R</i>	Steadman and Nuttall, (1963, 1964)
Most frequent morphologies	Truncated trigonal pyramid shape, plates needles (<i>3T</i>)		Cones or trigonally deformed cones (<i>1T</i>)	Ovoid based shape or columnar with rounded hexagonal or circular cross section (group D). Ovoid-to barrel-shaped morphology (<i>2H₂</i>)	Frondel, (1962); Hybler et al. (2000; 2002); Steadman and Nuttall, (1963); Kogure et al., (2001); Geiger et al. (1983)
Polytypes of trioctahedral T-O phyllosilicates	Non-MDO polytypes of cronstedtites : 9R Cornucopia mine (Nye Country, Nevada)				Frondel (1962)

575

576

Table 2

	Mg	Fe_{tot}	^{IV}Al	Si	^{IV}Fe	^{VI}Fe²⁺	^{VI}Fe³⁺
	0	3.79	0.02	1.19	0.79	2.18	0.81
	0.03	3.73	0.06	1.18	0.76	2.15	0.82
	0.02	3.68	0.09	1.20	0.70	2.18	0.80
	0	3.27	0.02	1.71	0.27	2.71	0.29
	0.10	3.54	0.19	1.17	0.64	2.07	0.83
	0.14	3.37	0.20	1.28	0.52	2.14	0.72
	0.03	3.71	0.11	1.15	0.74	2.12	0.88
	0.01	3.85	0.06	1.08	0.86	2.07	0.92
	0.01	3.73	0.04	1.22	0.74	2.21	0.78
	0.02	3.71	0.03	1.24	0.73	2.23	0.76
	0.01	3.81	0.02	1.16	0.82	2.15	0.84
	0	3.73	0.08	1.19	0.73	2.19	0.81
	0	3.89	0	1.11	0.89	2.11	0.89
	0.03	3.80	0.03	1.14	0.83	2.10	0.86
	0.07	3.35	0.27	1.31	0.42	2.24	0.70
	0	3.61	0.08	1.30	0.61	2.30	0.70
	0	3.84	0	1.16	0.84	2.16	0.84
	0.03	3.91	0.03	1.04	0.93	2.01	0.96
	0.06	3.59	0.10	1.25	0.65	2.19	0.75
	0	3.86	0	1.14	0.86	2.14	0.86
	0.04	3.89	0.03	1.04	0.93	2.00	0.96
	0.01	3.70	0.07	1.22	0.71	2.21	0.78
	0.02	3.82	0.07	1.10	0.84	2.08	0.90
	0.01	3.71	0.06	1.22	0.72	2.21	0.78
	0	3.77	0	1.23	0.77	2.23	0.77
	0	3.88	0	1.12	0.88	2.12	0.88
	0.01	3.76	0.05	1.18	0.77	2.18	0.82
	0.01	3.81	0.09	1.10	0.81	2.09	0.90
	0.06	3.27	0.28	1.38	0.33	2.32	0.61
Average	0.03	3.70	0.07	1.20	0.73	2.17	0.80
σ	0.03	0.18	0.08	0.13	0.16	0.13	0.13

578

579

Table 3

	Mg	Fe_{tot}	^{IV}Al	Si	^{IV}Fe	^{VI}Fe²⁺	^{VI}Fe³⁺
	0.01	3.74	0.07	1.18	0.75	2.17	0.82
	0.04	3.60	0.14	1.22	0.64	2.18	0.78
	0.04	3.59	0.15	1.21	0.63	2.17	0.79
	0.01	3.75	0.10	1.14	0.76	2.13	0.86
	0.04	3.53	0.26	1.17	0.58	2.12	0.84
Average	0.03	3.64	0.14	1.18	0.67	2.16	0.82
σ	0.02	0.10	0.07	0.03	0.08	0.03	0.03

580

Figure 1
[Click here to download Figure: Figure 1.eps](#)

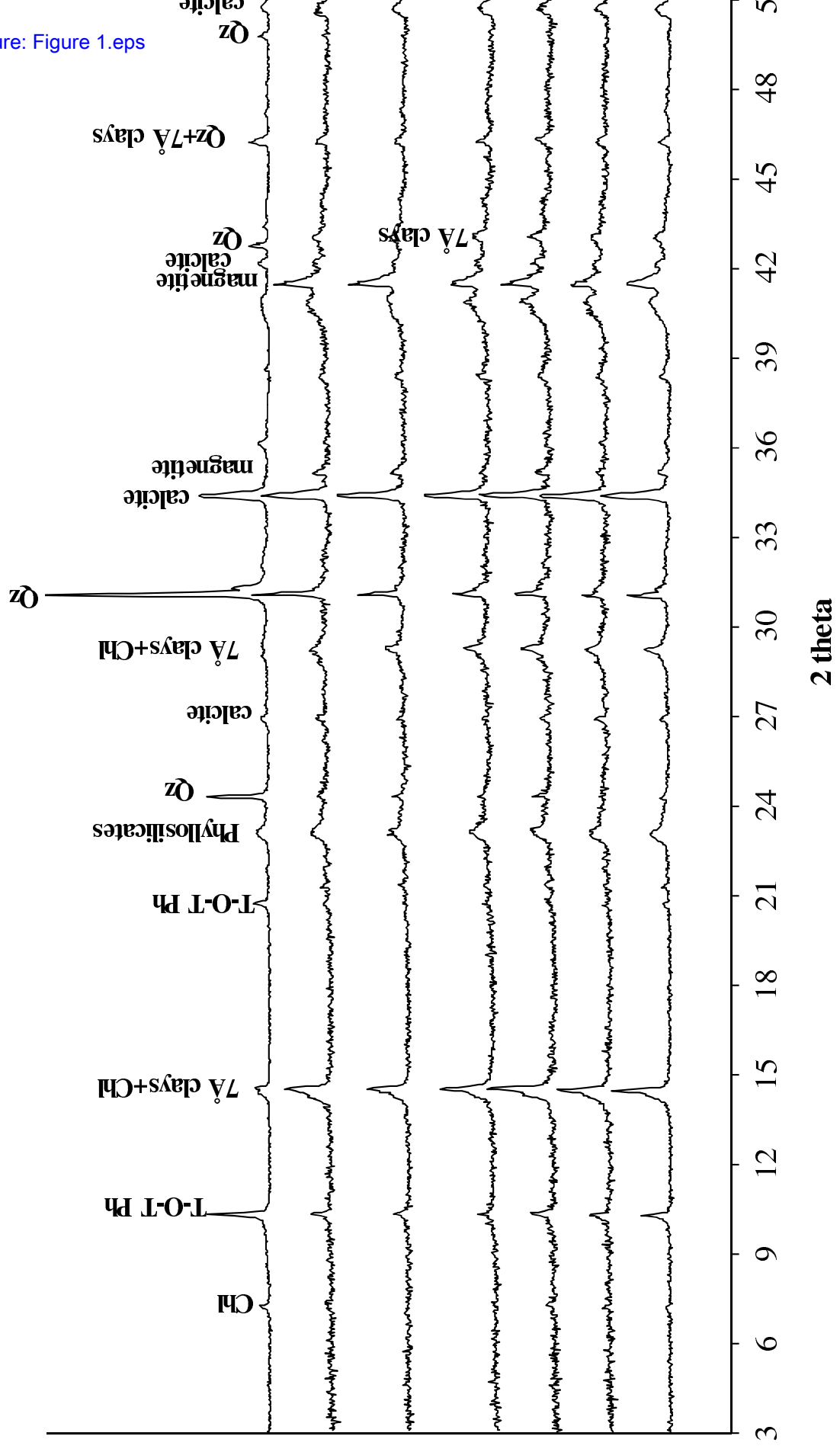


Figure 2
[Click here to download Figure: Figure 2.eps](#)

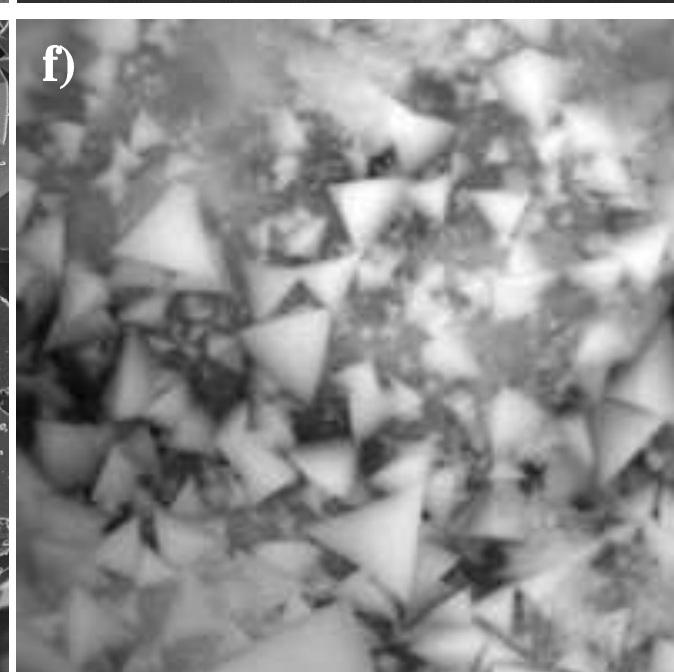
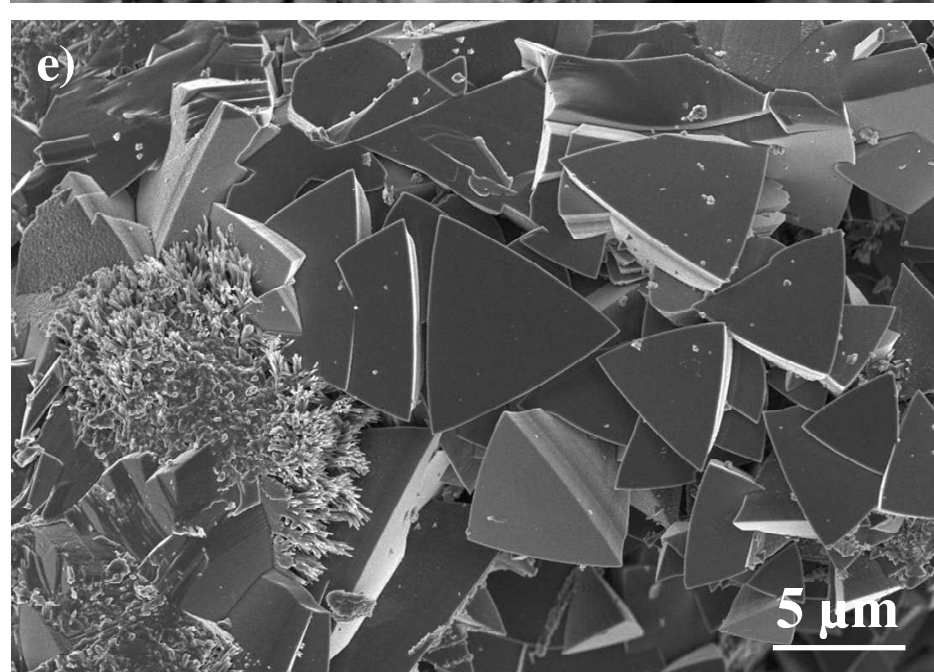
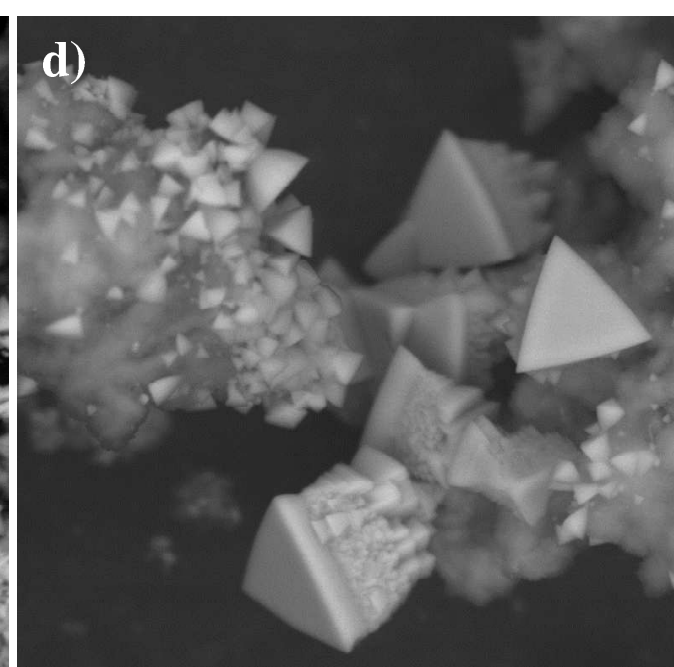
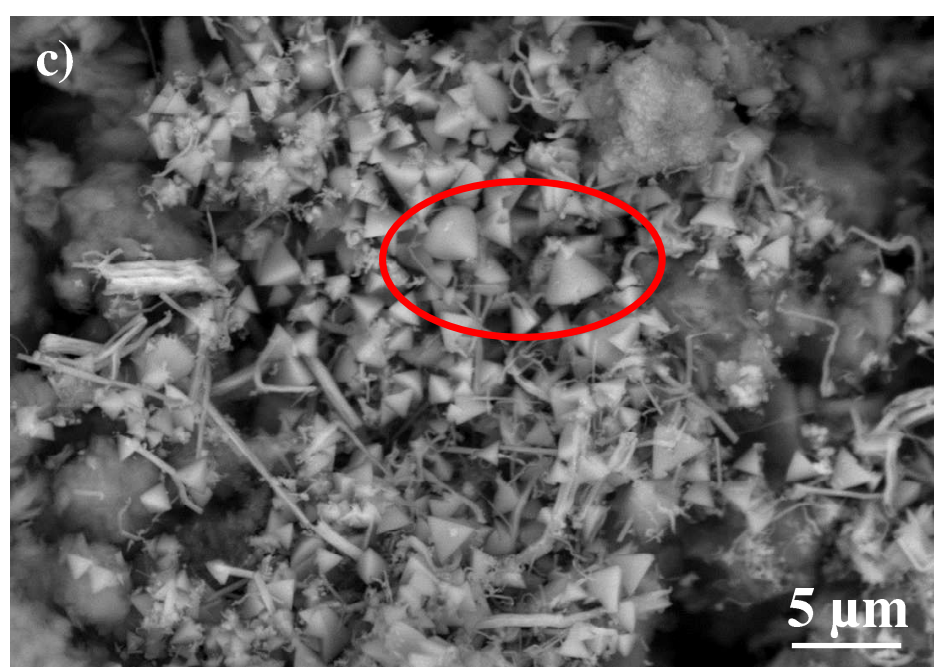
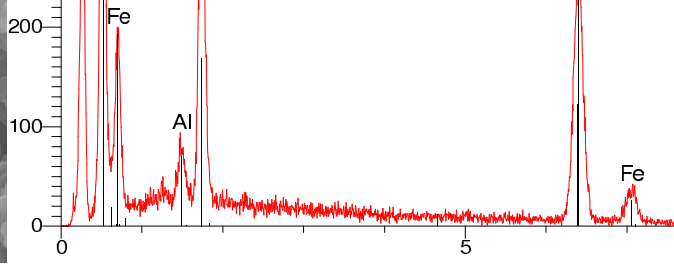
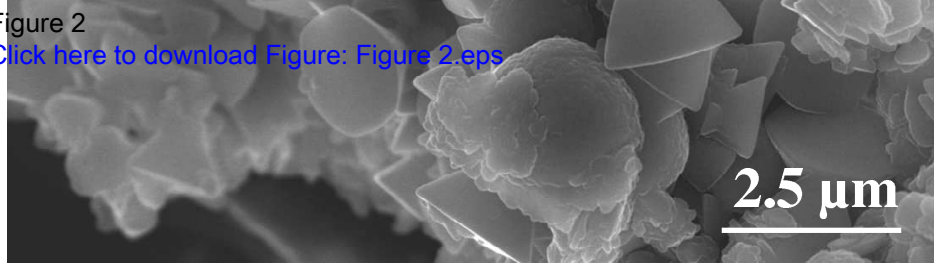


Figure 3

[Click here to download Figure: Figure 3 eps](#)

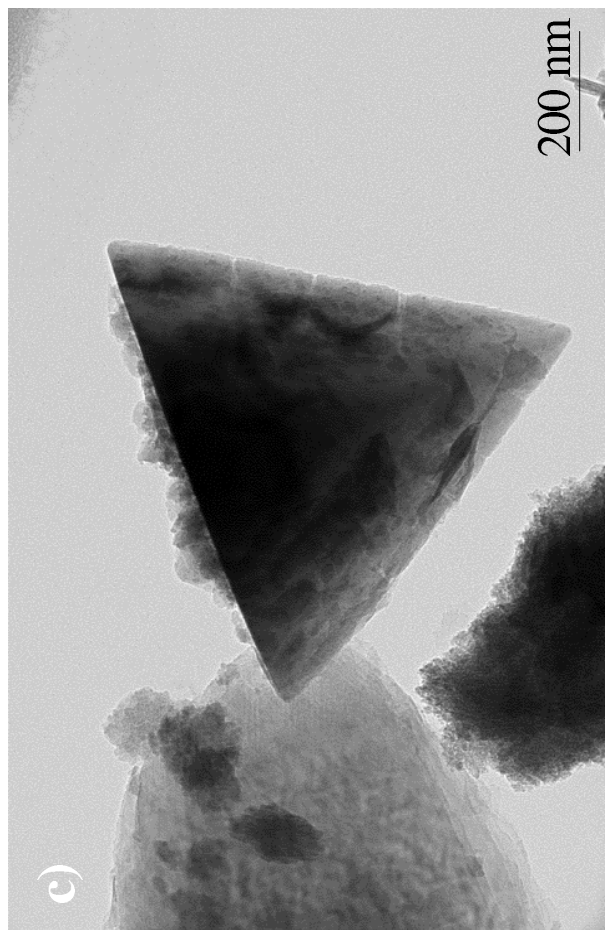
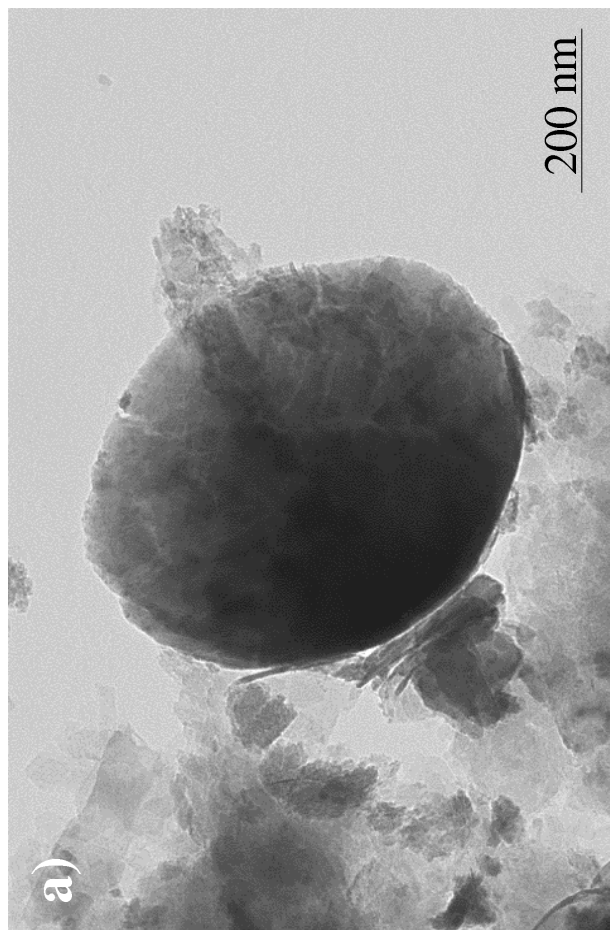
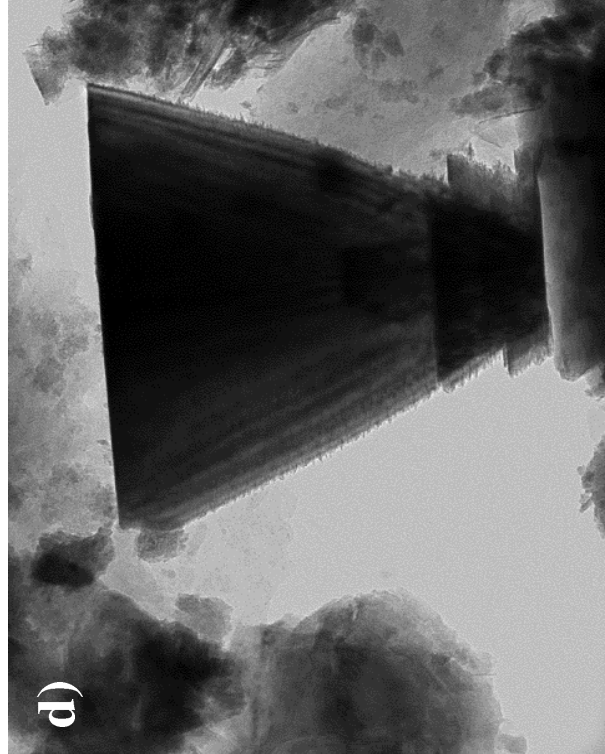
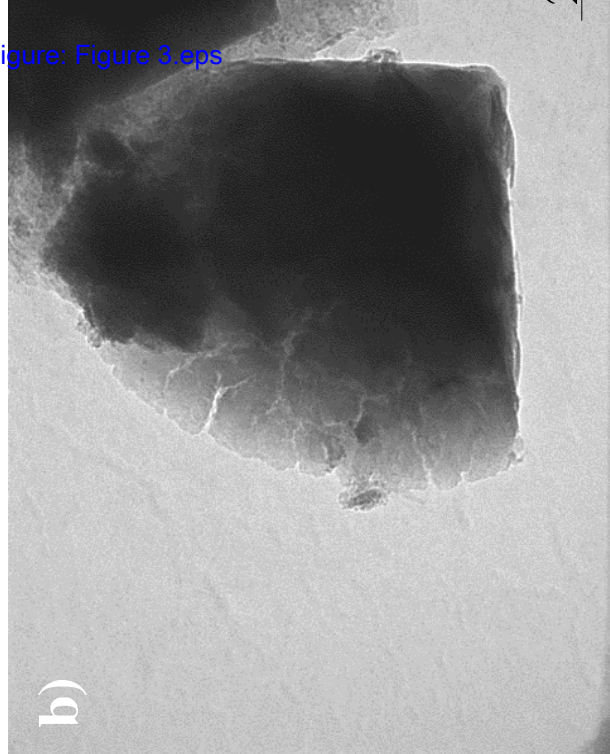


Figure 4

[Click here to download Figure: Figure 4.eps](#)

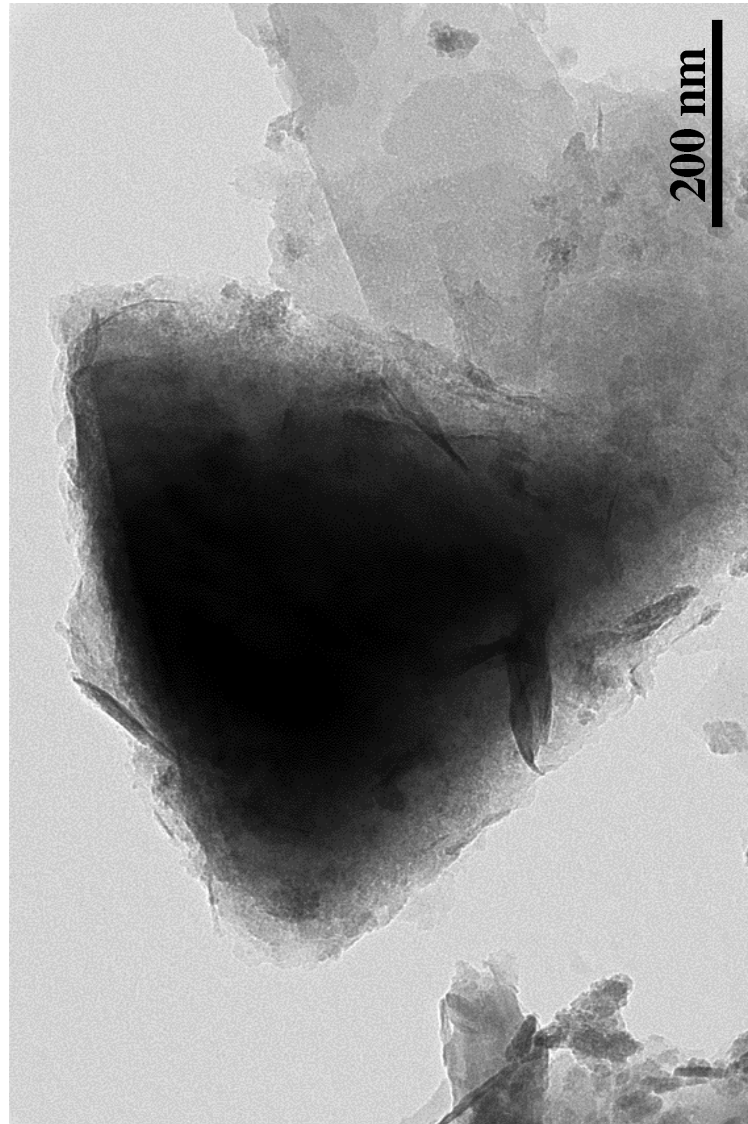


Figure 5

[Click here to download Figure: Figure 5.eps](#)

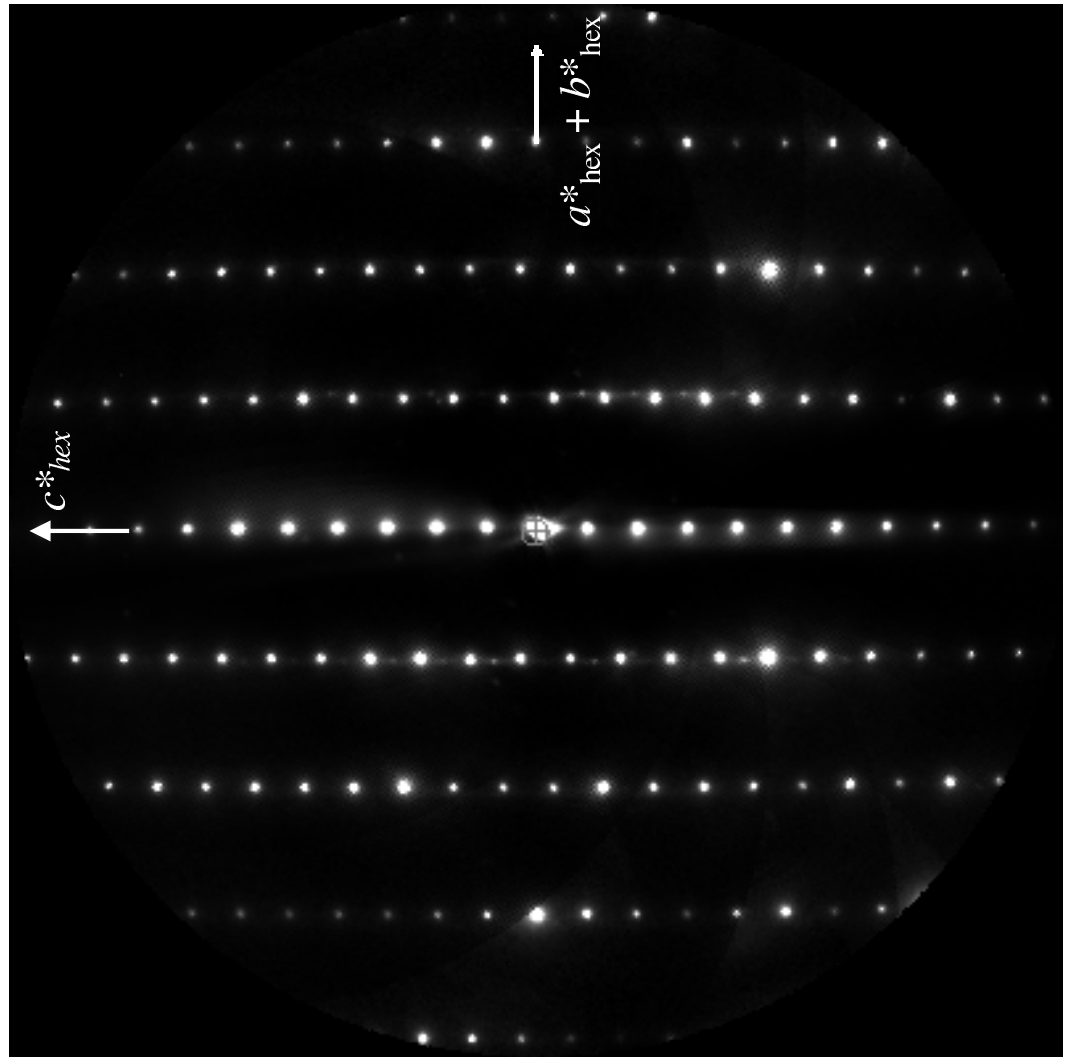


Figure 6

[Click here to download Figure: Figure 6.eps](#)

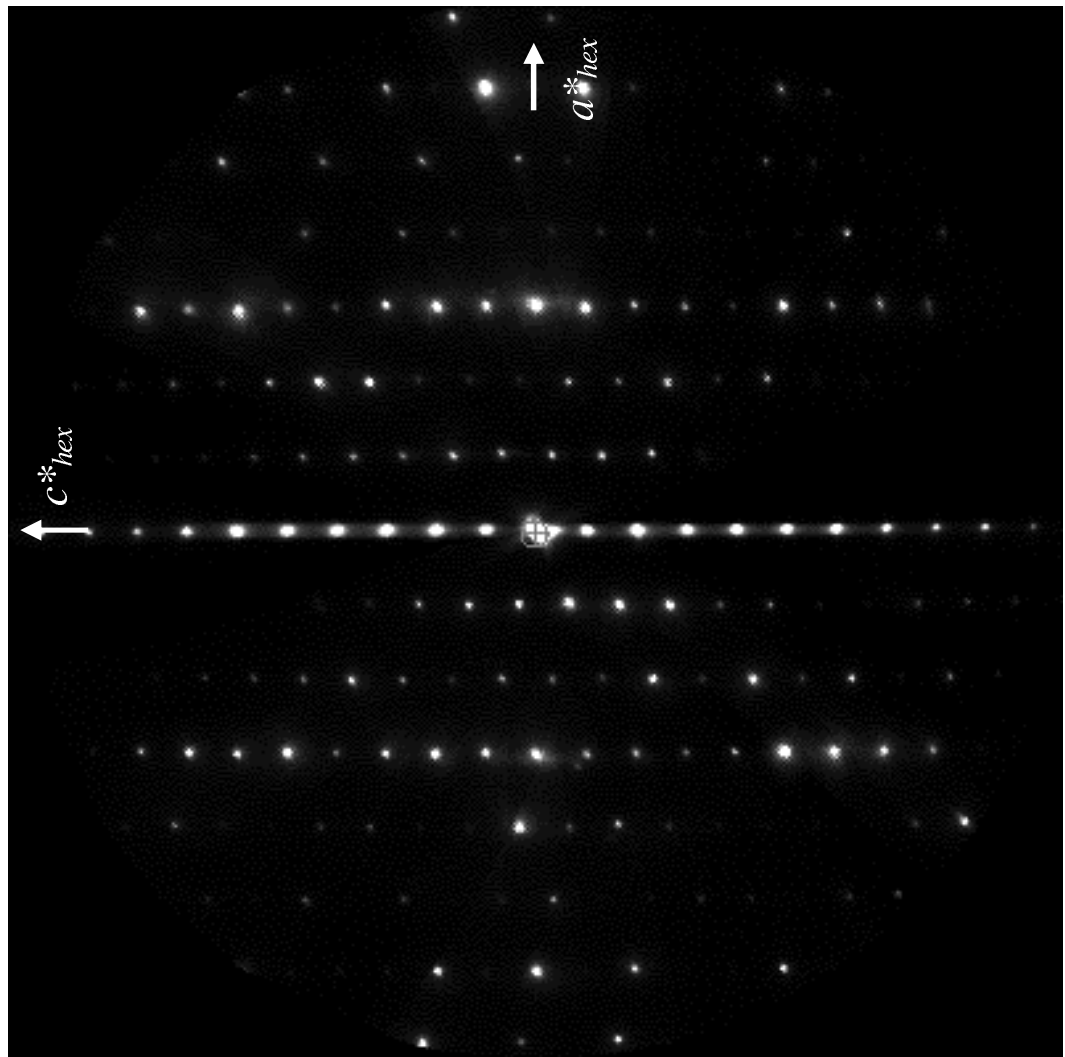
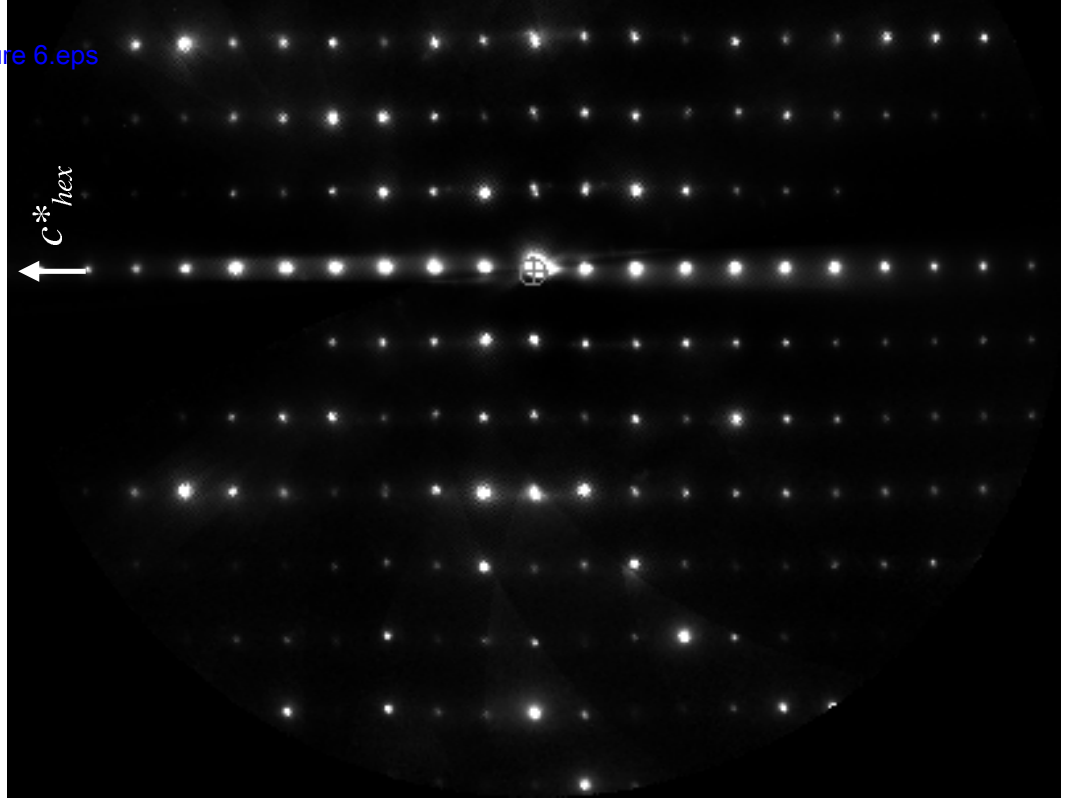


Figure 7
[Click here to download Figure: Figure 7.eps](#)

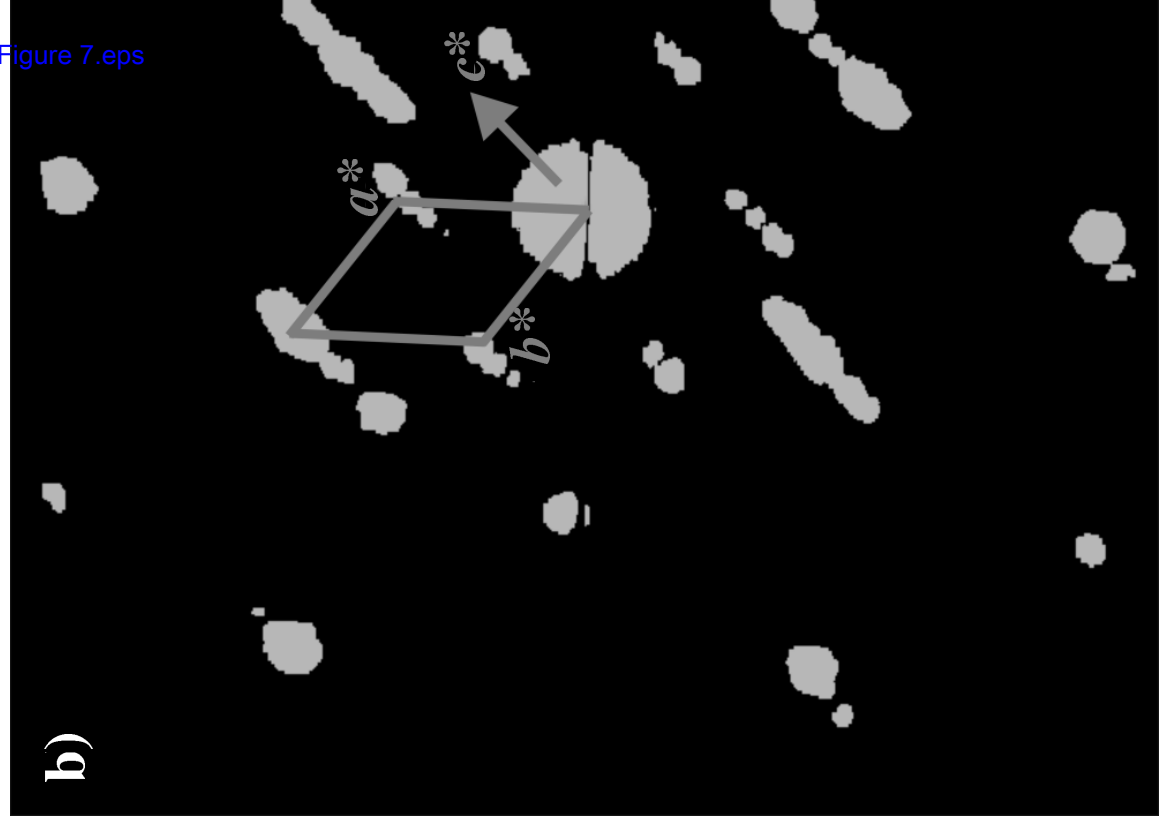
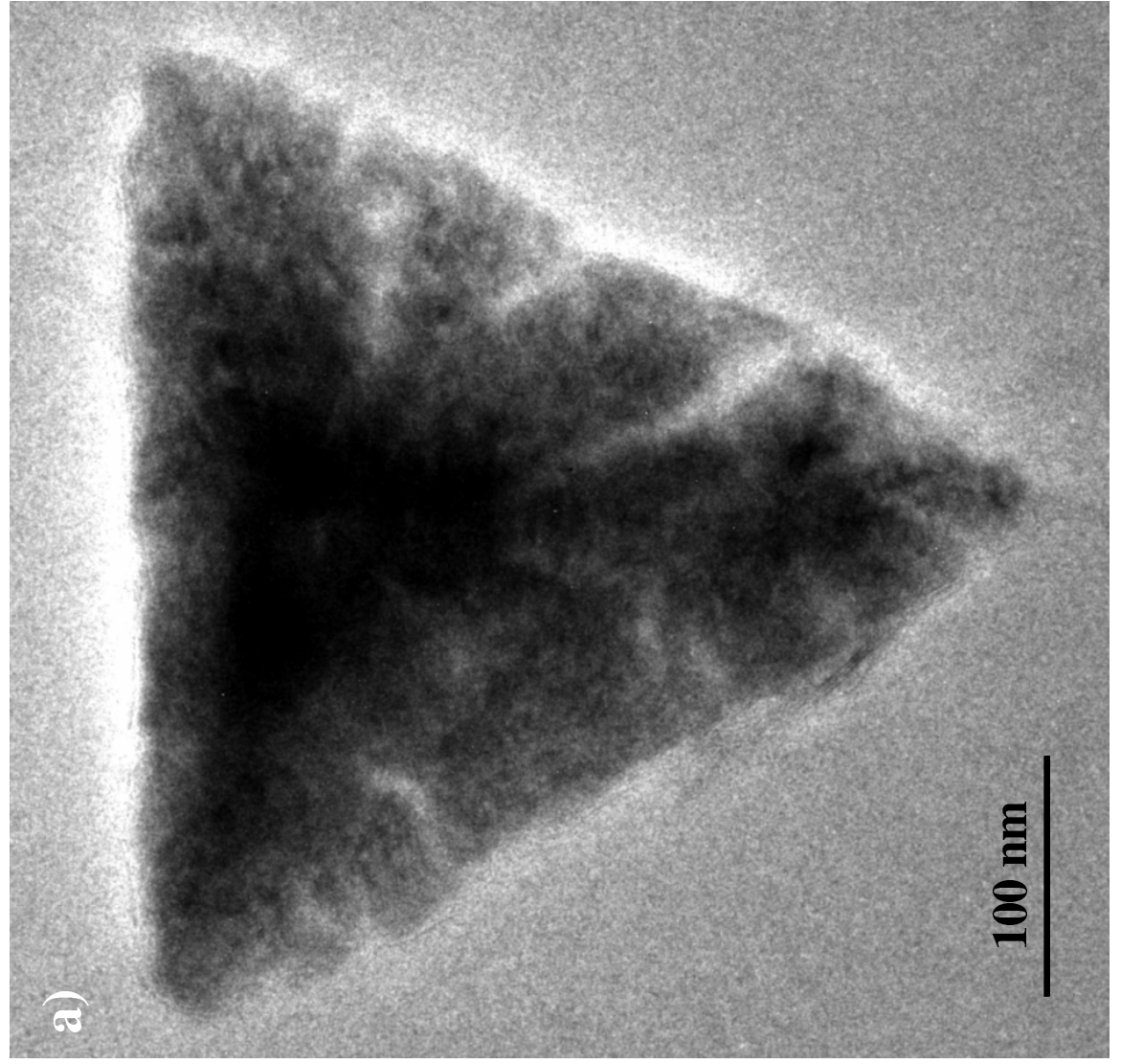


Figure 8
[Click here to download Figure: Figure 8.eps](#)

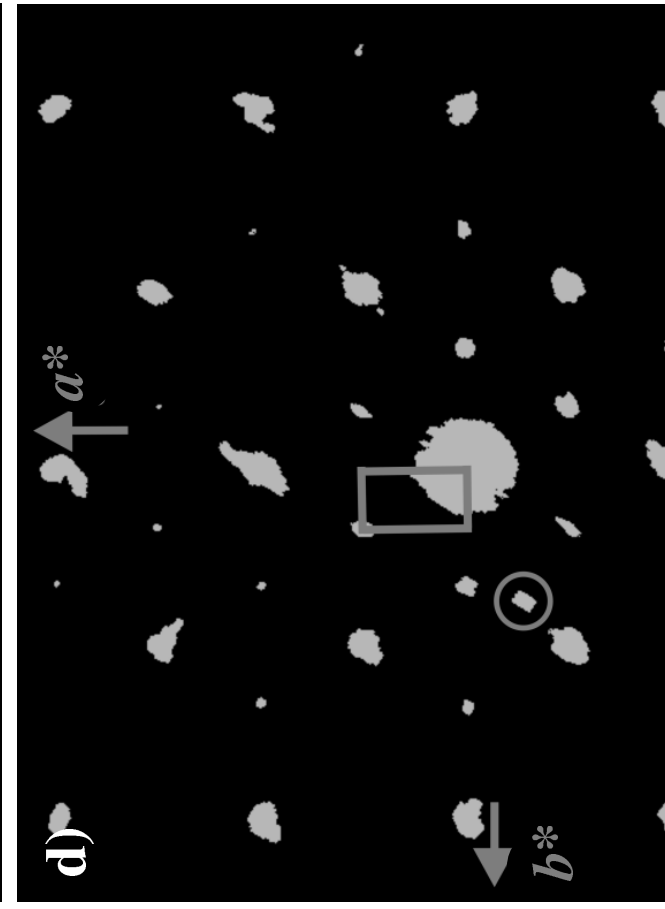
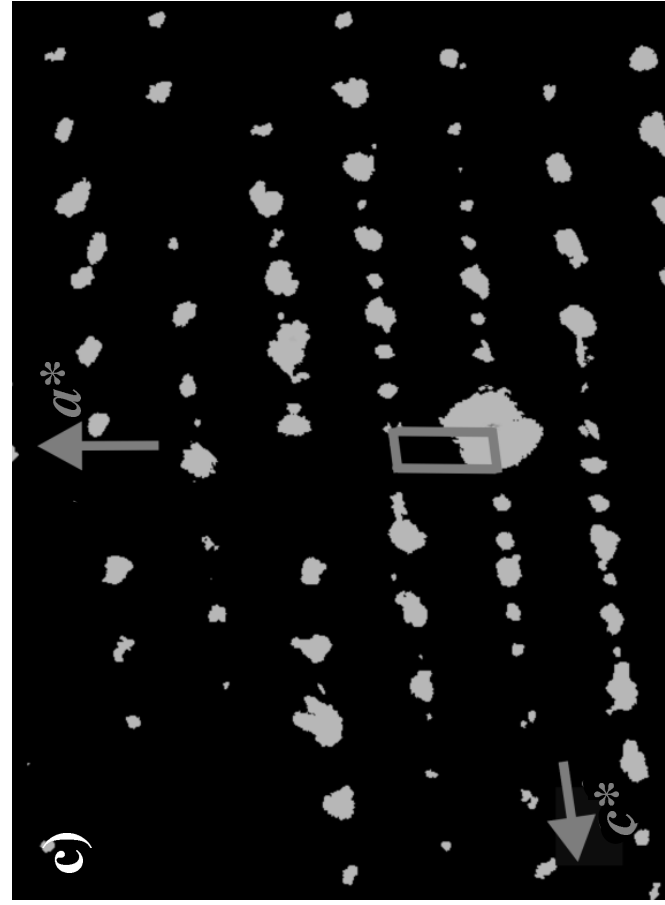
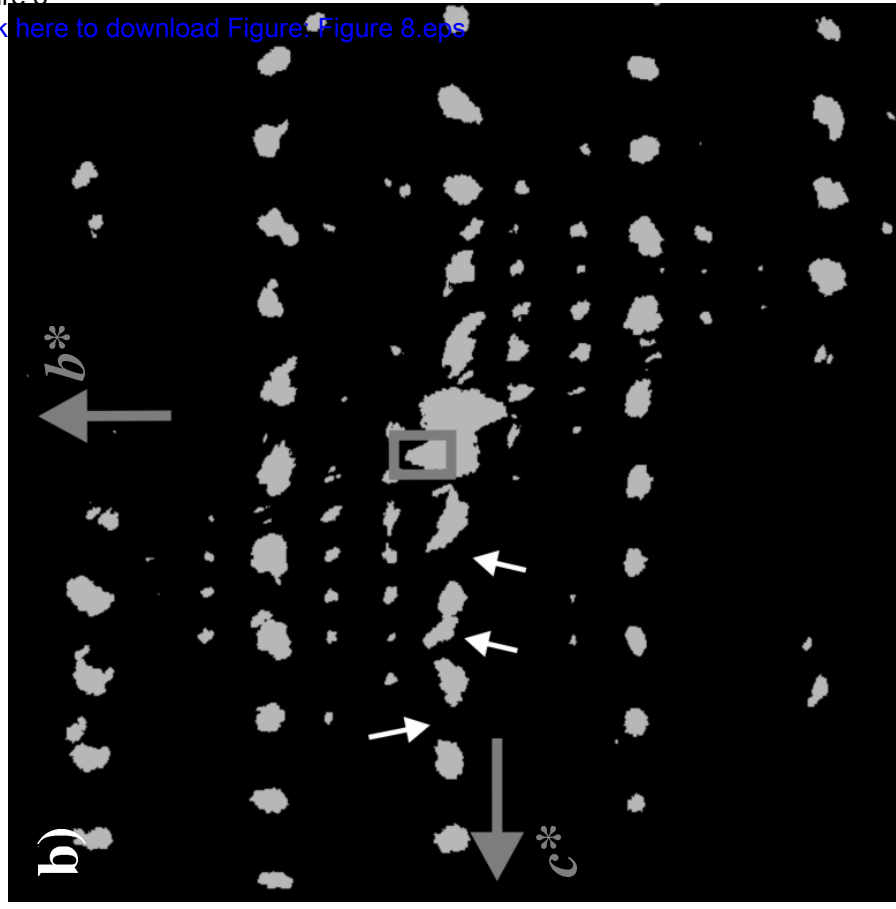
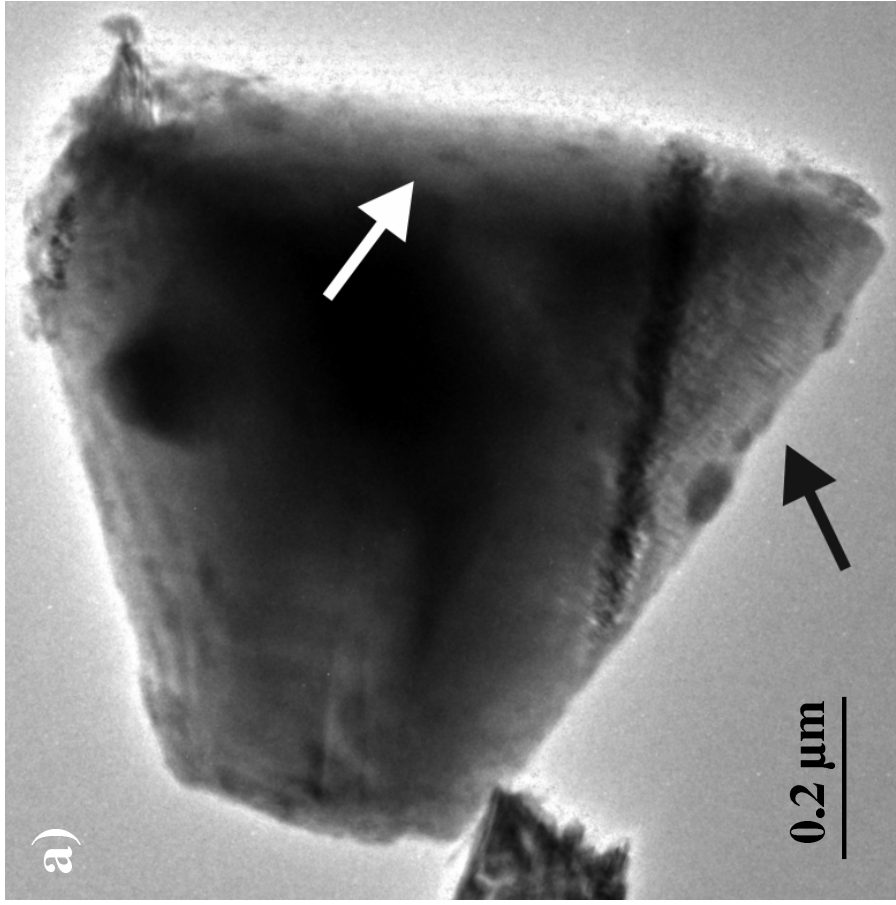


Figure 9
[Click here to download Figure: Figure_9.eps](#)

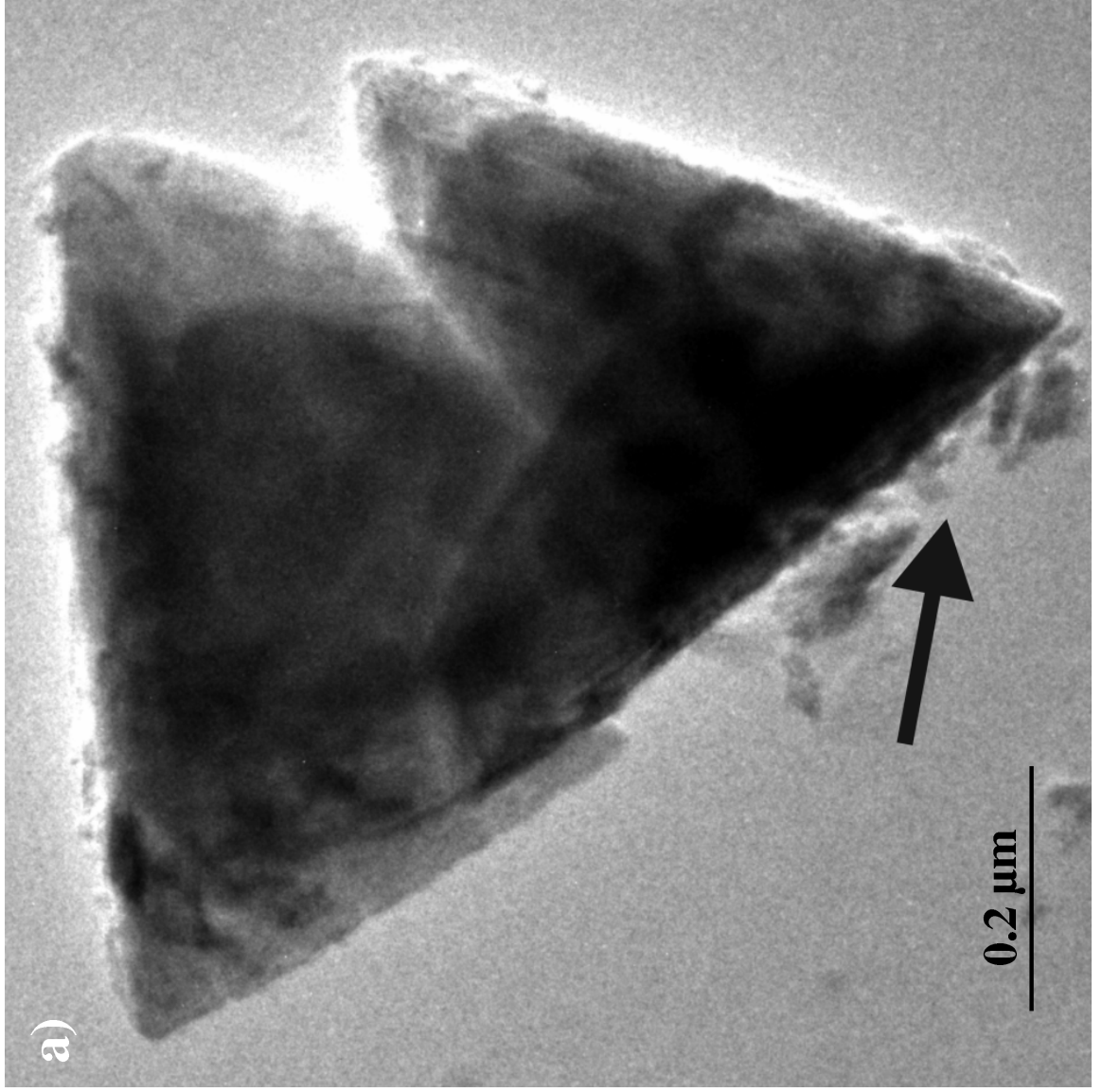


Figure 10

[Click here to download Figure: Figure 10.eps](#)

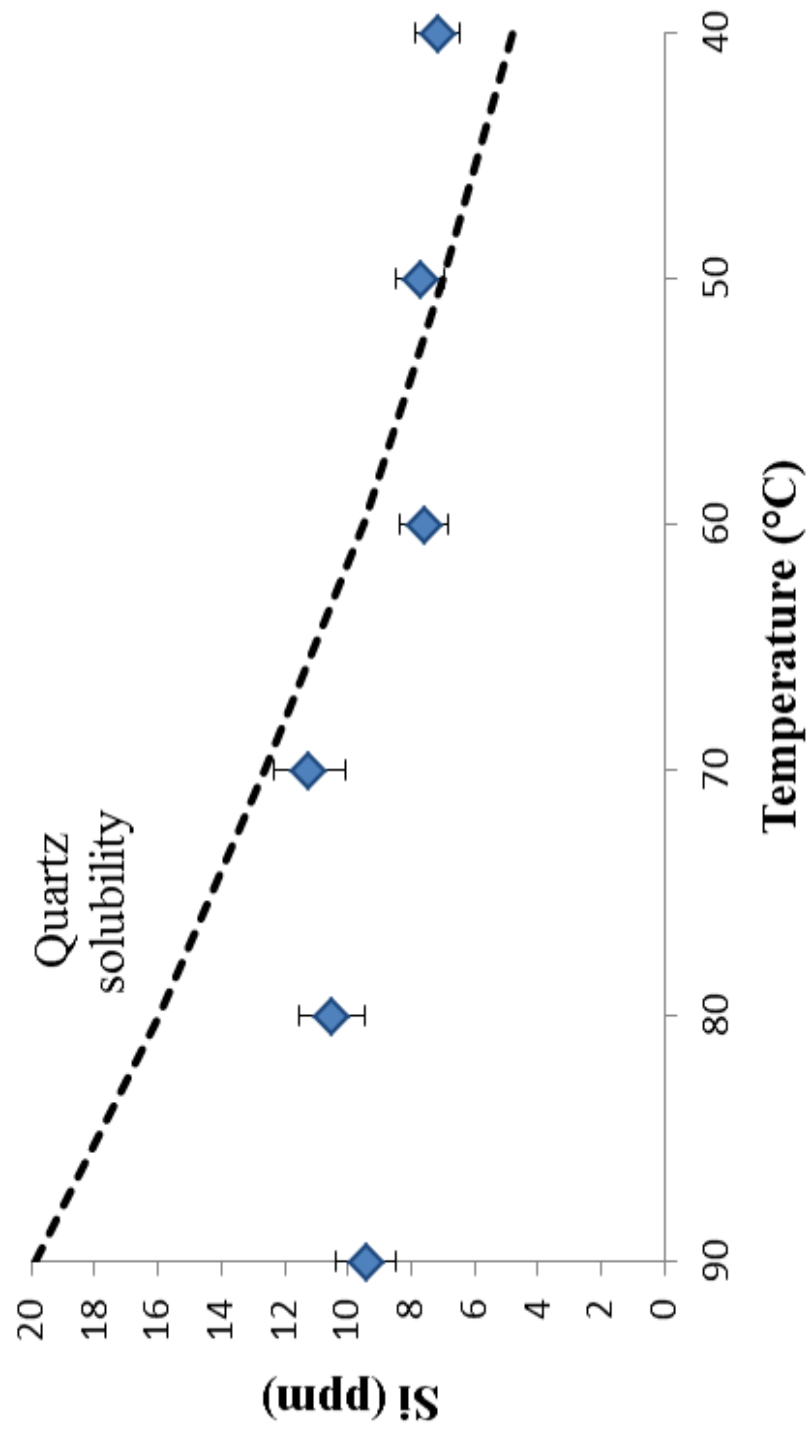


Figure 11
[Click here to download Figure: Figure 11.eps](#)

